

Assimilation of GPM-retrieved Ocean Surface Meteorology Data for Two Snowstorm Events during ICE-POP 2018

Xuanli Li¹, Jason B. Roberts², Jayanthi Srikishen³, Jonathan L. Case⁴, Walter A. Petersen², GyuWon Lee⁵, and Christopher R. Hain²

5 ¹University of Alabama in Huntsville, Huntsville, Alabama, USA

²NASA Marshall Space Flight Center, Huntsville, Alabama, USA

³Universities Space Research Association, Huntsville, Alabama, USA

⁴ENSCO, Inc./NASA SPoRT Center, Huntsville, Alabama, USA

10 ⁵Kyungpook National University, Daegu, Republic of Korea

Correspondence to: Xuanli Li (xuanli@nsssc.uah.edu)

For publication in Geoscientific Model Development

15 **Abstract.** As a component of the National Aeronautics and Space Administration (NASA) Weather Focus Area and Global Precipitation Measurement (GPM) Ground Validation participation in the International Collaborative Experiments for PyeongChang 2018 Olympic and Paralympic Winter Games (ICE-POP 2018) field research and forecast demonstration programs, hourly ocean surface meteorology properties were retrieved from the GPM microwave observations for January – March 2018. In this study, the retrieved ocean surface meteorological products – 2-m temperature, 2-m specific humidity, and 10-m wind speed were
20 assimilated into a regional numerical weather prediction (NWP) framework to explore the application of these observations for two heavy snowfall events during the ICE-POP 2018: 27-28 February, and 7-8 March 2018. The Weather Research and Forecasting (WRF) model and the community Gridpoint Statistical Interpolation (GSI) were used to conduct high resolution simulations and data assimilation experiments. The
25 results indicate that the data assimilation has a large influence on surface thermodynamic and wind fields in the model initial condition for both events. With cycled data assimilation, significantly positive influence of the retrieved surface observation was found for the March case with improved quantitative precipitation forecast and reduced error in temperature forecast. A slightly smaller yet positive impact was also found in the forecast of the February case.

30

1. Introduction

Cold season storms make great contributions to the global water cycle and influence local water supplies for household, agriculture, and manufacturing uses. In addition, winter sports tourism involving outdoor activities such as skiing, snowboarding, snowmobiling, ice fishing, etc., is a large market segment for mid to high latitude regions. On the other hand, hazardous winter weather including blizzards, ice storms, freezing rains, and heavy snow, often disrupt transportation, affect outdoor activities, cause delays and closures of airports, government offices, schools, and businesses, produce widespread and extensive property damages, losses of electricity, and present hazards to human health and even loss of life (Changnon, 2003, 2007; Call, 2010; FEMA, 2021; NOAA NCEI, 2021).

Accurate and timely forecast of the onset, duration, intensity, type, and spatial extent of precipitation is a major challenge in winter weather forecasting (Garvert et al., 2005; Ralph et al., 2005, 2010; Novak and Colle, 2012). These are especially important factors for providing support to ensure the success of highly weather-sensitive venues, such as the winter Olympic and Paralympic games that were held in South Korea during February and March 2018. Many factors can contribute to the development of winter precipitation, including synoptic forcing (e.g., warm advection, differential vorticity advection), strong baroclinicity in the presence of moisture sources (e.g., near coastlines), and large-scale environmental instability in the warm sector of a mid-latitude cyclone. For regions that contain complex terrain in proximity to large bodies of water (such as the Korean peninsula), local circulations and air-sea interactions also play important roles in determining the phase and amount of precipitation (Niziol et al., 1995; Kain et al., 2000; Schultz et al., 2002; O'Hara et al., 2009; Alcott and Steenburgh, 2010; Novak and Colle, 2012; Schuur et al., 2012; Novak et al., 2014; Roller et al., 2016).

In Korean peninsula, the weather and climate regime during the winter months is largely driven by the seasonal reversal of winds across eastern Asia and the western North Pacific Ocean from predominantly south/south-westerlies during the boreal summer months, to north/north-easterlies during boreal winter (Chang et al. 2006). The east Asian winter monsoon (EAWM) months are considered between November and March, and largely drive the temperature and precipitation patterns across Korea. The dominant weather features associated with the EAWM consist of a strong low pressure in the Aleutian region of Alaska, a cold-core Siberian-Mongolian High, and low-level northeasterly winds along the Russian east coast. Variability in the strength of the EAWM (described in Zhang et al. 1997) has been correlated to El Niño/Southern Oscillation phase (where La Niña [El Niño] corresponds to stronger [weaker] EAWM), and snowpack anomalies during the Autumn/Winter across Siberia, eastern Russia, and northeastern China (positive snowpack anomalies lead to stronger EAWM). A stronger EAWM corresponds to strong Aleutian lows, Siberian-Mongolian highs, a stronger subtropical jet stream across eastern Asia, and deeper troughs in eastern

Asia (Chang et al. 2006). Lee et al. (2010) found that, contrary to expectations, storm track activity is reduced during stronger EAWM and increased during weaker EAWM years.

70 Due to the prevailing EAWM regime, the Korean peninsula can feel the effect of severe winter weather in the form of rapidly-deepening mid-latitude cyclones and occasional cold surges from the Siberian-Mongolian semi-permanent high. Bomb cyclogenesis is most common along the Japanese coastline, but because of the Korean peninsula's proximity to the Yellow Sea (west) and Sea of Japan (east), strong baroclinicity can develop between the cold continental polar air over land and the warmer waters that provide abundant fluxes of heat and moisture into the atmosphere. Therefore, rapid deepening of cyclones can also occur in the vicinity of the Korean peninsula. In their satellite-era climatology of east Asian extratropical cyclones, Lee et al. (2020) showed that the Korean peninsula feels the influence of extratropical cyclones originating in three preferred regions: Mongolia, East China, and the Kuroshio current along the southern/eastern coast of Japan. Using reanalysis data back to 1958, Zhang et al. (2012) found similar results in terms of the common cyclogenesis regions affecting eastern Asia. Yoshiike and Kawamura (2009) found that while bomb cyclogenesis occurred slightly more frequently during weak EAWM years, it was more concentrated along the south-eastern Japan coast during strong EAWM, owing to larger heat fluxes over the Kuroshio current.

80 Locally-intense mesoscale cyclones have also been documented across the Sea of Japan, developing in response to polar outbreaks over the warmer waters in conjunction with the complex terrain along and north of the Korean peninsula. Tsuboki and Asai (2004) describe the process of strong convergence forming east of the Korean peninsula with substantial sensible and latent heating from the Sea of Japan leading to the formation of these mesoscale cyclones. Intense Sea of Japan cyclones can cause substantial wave activity and subsequent coastal damage along the east coast of Korea (Lee and Yamashita, 2011; Oh and Jeong, 2014; Mitnik et al., 2011), in addition to significant snowfalls across Korea. Clearly, an accurate representation of air-sea interactions in NWP models is important when forecasting the impacts of winter cyclones and accompanying heavy snowfalls across the Korean peninsula.

85 Numerous studies showed that in situ and remote sensed observations for surface conditions and the upper-atmosphere can provide a better description for both storm-scale processes and large-scale environments leading to improved precipitation forecasts (Zupanski et al., 2002; Cucurull et al., 2004; Zhang et al., 2006; Fillion et al., 2010; Hartung et al., 2011; Hamill et al., 2013; Salslo and Greybush, 2017; English et al., 2018; Zhang et al., 2019). In South Korea, data assimilation also indicated significant benefit for winter forecast (Kim et al., 2013; Kim and Kim, 2017; Yang and Kim, 2021). For example, Kim et al. (2013) demonstrated the assimilation of the conventional surface and upper air observations, aircraft, and multiple satellite observations located upwind or in the vicinity of the Korean peninsula into the Korea

Meteorological Administration (KMA) Unified Model. The result showed large decreases in the forecast error for the 24-, 36-, and 48-h forecasts of a strong winter storm event.

It is indicated that better representation of air-sea interaction from the ocean can provide benefit to the forecast of winter storms occurred in the downstream regions. For example, Peevey et al. (2018) showed a significant reduction in forecast error when dropsonde observations over Pacific Ocean were assimilated for winter storms in western United States. Therefore, it is of great interest to assimilate the observations over oceans surrounding the Korean peninsula and examine their impacts on winter storms affecting the peninsula. However, regular observations over these oceans are limited to only a few buoys, satellite observations and retrieved products that can provide a broad spatial coverage with regular revisit of the data sparse regions may be of substantial benefit.

In support of the International Collaborative Experiments for PyeongChang 2018 Olympic and Paralympic Winter Games (ICE-POP 2018) field campaign, special efforts were made to generate a set of near-surface ocean meteorology conditions (2-m air temperature, 2-m specific humidity, and 10-m wind speed) using the Global Precipitation Measurement (GPM) microwave observations from January to March 2018. In the satellite-based surface flux community (e.g. see Curry et al., 2004), significant efforts have been undertaken to estimate the near-surface meteorology from passive microwave observations to support the development of turbulent flux estimates from space. In particular, efforts have been made to estimate 2m air temperature and humidity (e.g., Jackson et al. 2006, Roberts et al. 2010, and Tomita et al., 2018) to complement long-standing wind speed estimates from microwave observation. However, the aforementioned efforts have almost explicitly focused on large-scale production of the fluxes for climatological analyses with long latencies. However, the surface retrieval products essentially provide similar measurements to those of buoys and generally with accurate performance. There is a long heritage of assimilating ocean surface buoy measurements within a data assimilation framework, but there has been little effort focused on assimilating the surface retrievals. This is part due to a lack of a real-time availability of these estimates and partly due to the focus on radiance-based assimilation system. The latter are not particularly tuned for leveraging lower-layer information in microwave observations as the stand-alone efforts originating from the satellite-derived flux community. The ICE-POP 2018 campaign provided a unique opportunity with near-real time passive microwave estimates of surface meteorology and a heavily observed regional environment to test the potential impact of assimilating wide-spread observations of near-surface meteorology. In this research, we explored the assimilation of this dataset using case studies with two snowstorm events occurred during the ICE-POP 2018 period. The objectives of the current research are to characterize the forecast ability of snowstorm events over complex terrain with the WRF model and further to develop and evaluate an approach to assimilate the passive microwave derived surface meteorology. Our focus herein emphasizes the large-

scale impacts of assimilation of the surface meteorology on the corresponding model fields and downstream forecast accuracy. Follow-on efforts will examine more on detailed physical processes (e.g. ocean evaporation, water and energy budget analyses, etc.) through which the assimilation impacts forecasts.

135

2. Data and Methods

2.1 *The GPM Retrieved Ocean Surface Meteorology Data for ICE-POP 2018*

The ICE-POP 2018 field campaign was led by the KMA as a component of the World Meteorological Organization (WMO)'s World Weather Research Programme (WWRP) Research and Development and Forecast Demonstration Projects (RDP/FDP) in order to enhance the capability of convective scale numerical weather prediction modeling and to improve the understanding of the high impact weather systems. The field campaign took place during the Winter Olympics (February-March) of 2018 in support of the 23rd Olympic Winter held in PyeongChang, Korea on 9-25 February and the 13th Paralympic Winter Games in 9-18 March 2018 which ran in real-time to provide guidance to forecasters during the Olympic Games. The focuses of the ICE-POP 2018 were to collect observations to measure the physics of heavy snow over the complex terrain in the PyeongChang region of South Korea and to improve the predictability of winter storm forecasting. During the ICE-POP 2018, remote sensing and in situ observations were collected with an intensive instrument network including enhanced surface weather stations, radiosondes and wind profilers. Cloud and precipitation processes were observed with four KMA S-band Doppler radars and an X-band Doppler radar, National Aeronautics and Space Administration (NASA) Dual Frequency Dual Polarimetric Doppler Radar (D3R), lidar, Precipitation Imaging Packages (PIP), Micro Rain Radars (MMR), Microwave Radiometers, Parsivel disdrometers, etc. An aircraft and a marine weather observing ship also deployed during the campaign (as detailed in Petersen et al. (2018)). Besides the remote-sensing data collected by NASA and KMA, high resolution ground-based in situ observation was also available. The South Korean Surface Analysis (SKSA) is a product interpolated from the observations collected by Automatic Weather Station (AWS) network in South Korea using a newly developed radial basis function (Ryu et al., 2020). This dataset provides surface temperature, moisture, wind, pressure, and precipitation amount over continental South Korean in Lambert Conic conformal projection with 1-km horizontal spatial resolution and 10-min time interval. This dataset was used in this study to evaluate the model performance and the impact of the data assimilation.

160

The GPM is an international mission led by the NASA and the Japanese Aerospace Exploration Agency (JAXA). The GPM contains a network of the GPM "Core" satellite and eight other constellation radiometers (e.g. Special Sensor Microwave Imager/Sounder (SSMIS), Advanced Microwave Scanning Radiometer 2 (AMSR-2), Microwave Humidity Sounder (MHS), etc.). From the core satellite and partner research and

165 operational microwave sensors, GPM provides a unified precipitation retrievals on real time and near-real
time over a large fraction of the globe (Hou et al. 2014; Skofronick-Jackson et al. 2017). As part of the NASA
Weather Focus Area and GPM support of the ICE-POP 2018 program, near-real-time ocean surface
turbulence flux retrievals were produced based on Roberts et al. (2010) using intercalibrated passive
170 microwave radiometer observations that were produced in support the Integrated Multi-SatellitE Retrievals
for GPM (IMERG) precipitation product (Berg et al., 2018). While intended to support precipitation
estimation, these brightness temperatures are also capable of supporting the estimation of the marine surface
meteorology — wind speed, sea surface temperature, air humidity and temperature — that are required to
estimate the surface turbulent fluxes. In this paper, we are interested in these near-surface atmosphere
conditions rather than the fluxes. The microwave imagers provide information on near-surface winds,
175 moisture, and temperature associated with the 10, 18.7, 23.8, 36.5, and 89¹ GHz vertical and horizontal
polarized microwave channels. These channels are used together with an a priori estimate of sea surface
temperature from the NCEP real-time global high-resolution (1/12°) sea surface temperature (RTG-SST)
product to retrieve 10-m wind speed, 2-m specific humidity, and 2-m air temperature, and sea surface
temperatures. The retrieval algorithm is based on a single-layer neural network following Roberts et al.
180 (2010). A large training dataset of standardized ocean buoy observations collocated within 1 hour and 25 km
of observations with each microwave sensor was developed. These data were broken into a training and set-
aside independent validation dataset with a 60% and 40% split, respectively. For training data, the data was
split into a training and cross-validation dataset with a 70% and 30% split. These retrieved parameters were
then used to estimate the surface turbulent fluxes through application of the Coupled Ocean–Atmosphere
185 Response Experiment (COARE) 3.5 (Edson et al., 2013) bulk flux algorithm. Compared to the independent
validation data, the root-mean-square (RMS) uncertainties are assessed at 1.1 g kg⁻¹, 0.9 K, and 1.2 m s⁻¹ for
surface humidity, temperature, and wind speed, respectively based on the mean statistics computed for GPM
Microwave Imager (GMI), Advanced Microwave Scanning Radiometer 2 (AMSR2), and the Special Sensor
Microwave Imager/Sounder (SSMIS) microwave imagers for which retrievals were developed. The retrievals
190 were essentially unbiased against the validation observations.

The GPM-retrieved surface observations are generally available over the oceans around the Korean peninsula within 1 h from 00, 06, 09, 12, 18, and 21 UTC on 7-8 March 2018. For February 27-28, the retrieved data are typically available within 1 h from 00, 06, 09, 15, 18, and 21 UTC. The coverage of the retrieval product varies with time due to the geolocation of the microwave imager swaths. At most of the

¹ Not all microwave imagers share the same central frequencies. However, each has a comparable channel near each of the bands listed.

195 above-mentioned times, observations typically cover $\sim 27^\circ - 50^\circ$ N over the Sea of Japan and the western North Pacific Ocean to the east of Japan. At 09, 18 and 21 UTC, Bohai Sea and Yellow Sea to the west of the Korean peninsula are usually observed or partly observed. Figure 1 shows an example of GPM-retrieved 2-m temperature, 2-m specific humidity, and 10-m wind speed at 09 UTC 7 March 2018 when the observations cover the west part of the Bohai Sea and Yellow Sea, most part of the Sea of Japan, and western
200 North Pacific Ocean. As this time, cold ($< -1^\circ\text{C}$) and dry ($< 3.0\text{ g kg}^{-1}$) air was observed at latitude above 44° N and warm ($> 17^\circ\text{C}$) and moist ($> 10.5\text{ g kg}^{-1}$) air at latitude lower than 30° N. Observed surface temperature ranges from $-7 - 23^\circ\text{C}$ and surface humidity from $0 - 13.5\text{ g kg}^{-1}$ over the model domain. Surface wind speed is found between $0 - 18\text{ m s}^{-1}$. Low wind centers appeared near the northern coast of Japan, one in central east Sea of Japan and the other one in western North Pacific Ocean.

205

2.2 Data Assimilation System and Numerical Experiments

Two heavy snowstorms affecting the Korean peninsula and ICE-POP field domain on 27-28 February and 7-8 March 2018 were selected for case studies. Figures 2 and 3 summarize the evolution of surface features for the two case studies. In both instances, a surface low pressure developed to the south and southwest of the
210 Korean peninsula and tracked to the northeast, passing along or just off the South Korea southern coast, placing the mountainous portions of South Korea, including the Olympics/Paralympics venue, in the favorable northwestern quadrant of the surface low for heavy snowfall. In the 27-28 February snowstorm, a closed 1005-hPa low is situated just off the eastern China coastline at 0000 UTC 28 February, to the southwest of the Korean peninsula, with another closed low over northeastern China at 1008 hPa (Fig. 2a).
215 The southern low experienced substantial deepening as it tracked northeastward over the next 24 to 36 hours, reaching extreme southern South Korea by 1200 UTC 28 February at 994 hPa intensity (Fig. 2b), the central Sea of Japan by 0000 UTC 1 March at 987 hPa and absorbing the northern low by this time (Fig. 2c), and then into northern Japan by 1200 UTC 1 March at 974 hPa minimum central pressure (Fig. 2d). The 28 February was the warmer of the two snowstorms, with most snow accumulation confined to the mountainous
220 terrain along the Korean east coast, including the Olympics venue, where storm-total snow accumulations of ~ 40 cm were observed (not shown). Gehring et al. (2020) analyzed the warm conveyor belt and microphysical characteristics of this heavy precipitation event, using datasets from the ICE-POP 2018 field campaign.

Temperatures were slightly colder during the 7-8 March event, resulting in a more widespread snowfall across the southern and eastern Korean peninsula within the mountains and at lower elevations. Following
225 the general synoptic snows, a surge of stronger north/northeasterly low-level winds off the Sea of Japan affected the Korean east coast and eastern mountains, leading to enhanced residual precipitation and strong orographic uplift (not shown). The 7-8 March extratropical cyclone began as a weak, open wave at 1200

UTC 7 March (Fig. 3a), then deepened to a 1010-hPa closed low to the southeast of the Korean peninsula at 0000 UTC 8 March (Fig. 3b). The cyclone slowly strengthened over the next 24 hours to 1004 hPa over the eastern Sea of Japan by 1200 UTC 8 March (Fig. 3c) and then to 1003 hPa as it tracked northeastward into northern Japan by 0000 UTC 9 March (Fig. 3d). An elongated meridional trough extended out of the low pressure center across much of Japan, resulting in a long fetch of north/northeasterly low-level winds across the Sea of Japan that affected the east coast of Korea during 8 March.

The Advanced Research Weather Research and Forecasting (WRF ARW; Powers et al., 2017) model was used to conduct the regional simulations for the two events. The snowstorms were simulated using 3-nested domains with horizontal resolution of 9-, 3-, and 1-km and 62 vertical levels as illustrated in Fig. 4. The model physics options include the Goddard long-wave and shortwave radiation schemes (Chou and Suarez, 1999), Grell-Freitas cumulus parameterization (Grell and Freitas, 2014), Mellor-Yamada-Janjic (MYJ) PBL schemes (Janjic, 1994), Morrison 2-moment microphysical scheme (Morrison et al., 2009) and Unified Noah land-surface model (Chen and Dudhia, 2001). The cumulus parameterization was only used for the outer 9-km resolution domain.

In the present study, the community Gridpoint Statistical Interpolation (GSI; Wu et al., 2002) v3.6 system was used to assimilate the GPM-retrieved ocean surface meteorology data. The GSI system was initially developed by the NCEP Environmental Modeling Center (EMC) and is currently maintained and supported by the National Oceanic and Atmospheric Administration (NOAA) Development Testbed Center (DTC; Hu et al., 2016). The GSI is built in physical space for a unified, flexible, and efficient modular system for multiple parallel computing environments and has been implemented real-time into both global and regional data assimilation (Wu, 2005; De Ponte et al., 2007; Kleist, 2009). The community GSI is functionally equivalent to the operational version used in NCEP. The system readily incorporates multiple types of observational data including conventional data, radar, and satellite radiance and retrieved products.

The GSI system is a 3-dimensional variational (3DVAR) data assimilation system (more detailed description in Wu et al., (2002)). In GSI, the 3DVAR cost function \mathbf{J} is defined by the following equation:

$$\mathbf{J} = \mathbf{J}_b + \mathbf{J}_o + \mathbf{J}_c = 1/2 [\mathbf{x}^T \mathbf{B}^{-1} \mathbf{x} + (\mathbf{H}\mathbf{x} - \mathbf{y})^T \mathbf{R}^{-1} (\mathbf{H}\mathbf{x} - \mathbf{y})] + \mathbf{J}_c \quad (1)$$

where \mathbf{x} is the analysis increment ($\mathbf{x}_a - \mathbf{x}_b$), \mathbf{x}_a is analysis fields, \mathbf{x}_b is background fields, \mathbf{J}_c is constraint terms, \mathbf{B} is the background error covariance matrix for analysis control variables, $\mathbf{y} = \mathbf{y}_{\text{obs}} - \mathbf{H}\mathbf{x}_b$ is the observation innovation, \mathbf{R} is the observational error covariance matrix, and \mathbf{H} represents a transformation operator from the control variables to the observations. The control variables in GSI include stream function, unbalanced velocity potential, unbalanced virtual temperature, unbalanced surface pressure, and pseudo relative humidity. The background error covariance is an important factor for a successful data assimilation. The GSI package

260 comes with pre-computed files for **B**. To obtain a more accurate regional data assimilation result, we used the “gen_be” package in the WRF Data Assimilation (WRFDA) system to compute a domain-specific **B** using the “NMC method” (Parrish and Derber 1992) with 1 month of WRF 24-h and 12-h forecasts for all model domains. **B** matrix provides model error statistic including the vertical and horizontal length scales and regression coefficients for the control variables.

265 Table 1 lists the numerical experiments and corresponding data assimilation activities performed for the two cases. Two different numerical experiments were conducted for each snowstorm event. For the March 7-8 case, the control experiment (CTRL_Mar) assimilates the conventional prepbufr observations every 6-h using the prepbufr data obtained from the National Center for Atmospheric Research (NCAR) Research Data Archive (available at <http://rda.ucar.edu/data/ds337.0>). The conventional data refers to the global surface and
270 upper air observation operationally collected by the National Centers for Environmental Prediction (NCEP) which includes surface, marine surface, radiosonde, pibal and aircraft reports from the Global Telecommunications System (GTS), profiler, United States radar derived winds, SSM/I oceanic winds and total precipitable water retrievals, and satellite wind report data from the National Environmental Satellite
275 Data and Information Service (NESDIS). Another experiment, DA_Mar, assimilates the GPM-retrieved ocean surface temperature, specific humidity, and wind speed observations besides the conventional prepbufr data. As shown in Table 1, cycled assimilation of the GPM-retrieved ocean surface meteorology data was performed at 06, 09, 12, 18, and 21 UTC of 7 March and 00, 06, 09, 12, 18, and 21 UTC 8 March based on the availability of the retrieval product. Both experiments began at 00 UTC 7 March 2018 and ended at 00 UTC 9 March 2018. For both experiments, the initial and boundary conditions of the WRF background field
280 were interpolated from the 0.5° resolution Global Forecast System (GFS) analysis. For the 27-28 February 2018 event, CTRL_Feb and DA_Feb were conducted with settings similar to CTRL_Mar and DA_Mar, respectively. Both experiments started at 00 UTC 27 February 2018 and ended at 00 UTC 1 March 2018. For DA_Feb, the GPM-retrieved ocean surface meteorology data was assimilated at 06, 09, 15, 18, and 21 UTC of 27 February and 00, 06, 09, 15, 18, and 21 UTC 28 February 2018.

285

3. Results

In this section, the numerical experiments with and without assimilation of the GPM-retrieved surface products were compared with the observations collected for the March 7-8 and February 27-28 snowstorm cases. The impact of the data on initial conditions and short-term forecasts are examined.

290

3.1. Case study for March 7-8 Snowstorm Event

In order to illustrate the overall distribution of the GPM-retrieved surface observations and the difference

between from the background, Fig. 5a-c shows the scatterplot of 2-m temperature, 2-m specific humidity, and 10-m wind speed observations with respect to the departures between the observed values and WRF background (i.e., a positive departure represents a higher value in observation than the model). As a pre-
295 process step before data assimilation, outliers with magnitude of surface temperature departure $> 6\text{ }^{\circ}\text{C}$, specific humidity departure $> 4\text{ g kg}^{-1}$, or wind speed departure $> 9\text{ m s}^{-1}$ were removed. For the observations used for the two cases, the median values are $10.59\text{ }^{\circ}\text{C}$, 6.47 g kg^{-1} , and 8.43 m s^{-1} for surface temperature, specific humidity, and wind speed. The 25th (and 75th) percentile values of the observed surface temperature, specific humidity and wind speed are 4.96 (and 16.71) $^{\circ}\text{C}$, 4.06 (and 8.70 g kg^{-1}), and 6.04 (and 10.74 m s^{-1}), respectively, which indicates that a larger part of the observational data located at the south part of Sea of Japan and western North Pacific Ocean than the north part. The probability density functions (PDF) of the departures of 2-m temperature, 2-m specific humidity, and 10-m wind speed are shown in Fig. 5d-f. An apparent skewness to the positive side is shown in the PDF of the surface temperature departure (Fig. 5d)
300 with the mean (and standard deviation) of 1.19 (and 1.75) $^{\circ}\text{C}$. For surface specific humidity, the departure shows a narrower spread with 95% of the values ranging from -2 to 2 g kg^{-1} . The PDF of the surface specific humidity departure skews to the negative side with the mean and standard deviation of -0.41 and 0.89 g kg^{-1} . This indicates a generally colder model atmosphere with higher specific humidity at ocean surface in the WRF background when compared to the observations. For surface wind speed, the departure has 98% of the values between -5 and 5 m s^{-1} . The mean and standard deviation for the surface wind speed departure is 0.33 and 2.02 m s^{-1} , respectively.
310

Through data assimilation, the GPM-retrieved surface observation directly influences the thermodynamic and wind fields of the WRF initial condition. Figure 6 displays surface condition of the March 7-8 case before and after the data assimilation cycle at 09 UTC 7 March 2018. Since specific humidity is not one of the GSI control variables and specific humidity is a function of temperature and water vapor mixing ratio, the observed specific humidity was converted into relative humidity in Fig. 6 for a more direct view on data
315 assimilation impact. The difference between the data assimilation analysis and the model background field (analysis – background, or "A – B", the increment added to the model field after data assimilation, in Fig. 6c, 6f, and 6i) was compared with the difference between the observation and the model background (observation – background, or "O – B", in Fig. 6b, 6e, and 6h) to indicate the changes in surface temperature, relative humidity, and wind speed fields by data assimilation. Before the data was assimilated, surface temperature in background was generally lower than the observation over Bohai Sea, Yellow Sea, and Sea of Japan which is reflected by the areas of positive O – B with the magnitude up to $6\text{ }^{\circ}\text{C}$ (Fig. 6b). High O – B values were also found over western North Pacific Ocean at latitudes above 38° N . After data assimilation, an increase
320 was made in surface temperature indicated by positive A – B over Bohai Sea and Yellow Sea, and generally
325

positive A – B over Sea of Japan and western North Pacific Ocean (Fig. 6c) where positive O – B was found. For surface relative humidity, the background was more humid than the observation over eastern and central Sea of Japan and drier than the observation in the west part close to the coast of North Korea. Over western North Pacific Ocean, O – B was generally negative with magnitude down to 30%, except a few positive spots at latitudes above 40° N (Fig. 6e). After data assimilation, surface relative humidity has decreased by up to 20% over a large part of western North Pacific Ocean and east Sea of Japan. An increase was created with positive A – B over west Sea of Japan (Fig. 6f). For surface wind speed, the background is apparently lower than observation at northern Sea of Japan and northern part of western North Pacific Ocean and generally higher than observation at central to southern Sea of Japan and southern part of western North Pacific Ocean for latitude below 40° N (Fig. 6h). After data assimilation, A – B generally agrees with the pattern shown in O – B with positive wind speed increment at regions with positive O – B and negative increment at regions with negative O – B (Fig. 6i). The Root Mean Square Difference (RMSD) was also calculated for O – B and A – B at locations where the observational data is valid. RMSD is 2.35 °C, 8.12%, and 4.16 m s⁻¹ for O – B in surface temperature, relative humidity, and wind speed, respectively. For A – B, RMSD is 1.36 °C, 4.01%, and 1.83 m s⁻¹, indicating an effective assimilation of the observational data was made to the WRF initial condition.

With the initial condition provided from data assimilation, the WRF forecast began. During the model integration, some of the changes in the initial condition were enhanced and some of the changes were reduced by the model dynamic adjustment. Therefore, it is important to understand how long and by how much the data impact will last in model forecast. Fig. 7a shows the RMSD in surface temperature, surface specific humidity, and surface wind speed between DA_Mar and CTRL_Mar calculated over the entire model domain for 0-6 h forecast after the 5th data assimilation cycle conducted at 21 UTC 7 March 2018. At 21 UTC, domain-averaged RMSD is 1.14 °C, 0.41 g kg⁻¹, and 1.72 m s⁻¹ for surface temperature, specific humidity, and wind speed, respectively. After the first hour of integration, the RMSD showed a rapid decline to 0.95 °C, 0.35 g kg⁻¹, and 1.66 m s⁻¹ which is 17%, 15%, and 4% reduction of the original values at the analysis time. In the next 5 hours' integration, these values dropped slowly to 0.78 °C, 0.29 g kg⁻¹, and 1.59 m s⁻¹, corresponding to additional 14%, 15%, and 4% reduction. Fig. 7b-d provides the vertical profiles of RMSD of temperature, specific humidity, and wind speed calculated over the entire model domain. Profiles T, Q, and WSPD represent the RMSD values at 61 model vertical levels at 21 UTC and T1, Q1, WSPD1 are for 22 UTC 7 March 2018. After 1 h time integration, Fig. 7b shows a sharp decrease in temperature RMSD at low level atmosphere below model level 20 (~ 850 hPa). For specific humidity, Fig. 7c indicates a decrease in RMSD in boundary layer below model level 8 (~ 925 hPa) and an increase in mid-level atmosphere from model level 20 to 38 (~ 600 hPa). From 21 UTC to 22 UTC, an apparent decrease in the wind speed RMSD

was found (Fig. 7d) from model level 10 (~ 925 hPa) to high level atmosphere at model level 50 (~ 300 hPa).

360 The impact of the cycled assimilation of the GPM-retrieved data on surface temperature forecast was examined. Table 2 lists the Root-Mean-Square error (RMSE) of 2-m temperature calculated every 6-h across continental South Korea from 12 UTC 7 March to 00 UTC 9 March using the South Korean Surface Analysis as the reference dataset. From 12 UTC 7 to 00 UTC 8 March, the RMSE values in DA_Mar were close to those in CTRL_Mar (i.e., 0-0.01 °C difference). After the 7th cycle of data assimilation at 06 UTC 8 March, 365 RMSEs in DA_Mar were consistently smaller than CTRL_Mar. At the end of the model simulation time, surface temperature RMSE in DA_Mar was 2.14 °C which is 0.33 °C lower than CTRL_Mar. Figure 8 shows an example of 2-m temperature from the South Korean Surface Analysis compared with CTRL_Mar and DA_Mar at 15 UTC 8 March 2018. Generally, surface temperature was around 0-4 °C at this time over South Korea with a few warmer areas of 4-6 °C along the southeastern coast and Jeju Island. Colder temperature (- 370 2°C) was observed in the Taebaek Mountains with a few spots below -4 °C (Fig. 8a) in the northern tip of Gangwon province. Both CTRL_Mar and DA_Mar predicted colder temperature than the observation in South Korea. This is especially apparent along the Taebaek Mountain range where temperature below -4 °C was produced in DA_Mar and below -6 °C in CTRL_Mar. Over Sobaek Mountains, temperature below -2 °C was produced in DA_Mar and below -4 °C in CTRL_Mar, which were 2-4°C colder than the observation. 375 Comparing with DA_Mar, CTRL_Mar produced a much larger area with temperature below 0 °C and apparently colder temperature along the Taebaek Mountains. The RMSE of 2-m temperature calculated at this time confirms the conclusion in Fig.8 with 2.89 °C in CTRL_Mar and 2.03 °C in DA_Mar.

The impact of the GPM-retrived ocean surface data on precipitation forecast was shown in Fig. 9. 1-h precipitation observed by the South Korean Surface Analysis at 16 UTC 7 March 2018 was compared with 380 the results from CTRL_Mar and DA_Mar. At this time, light snowfall was broadly observed over northern to central South Korea. The storm started to produce heavier snowfall in the southern region with >3 mm h⁻¹ in the southwestern tip of the Korean peninsula and >8 mm h⁻¹ in Jeju Island. From Fig. 9b and 9c, it is indicated that the simulated storm in both DA_Mar and CTRL_Mar also produced light to moderate snowfall over most area of South Korea with heavier precipitation above 3 mm h⁻¹ over the South Jeolla Province. The 385 pattern of precipitation in DA_Mar is very similar to CTRL_Mar. Strong precipitation above 10 mm h⁻¹ was predicted in Jeju Island in both CTRL_Mar and DA_Mar. Comparing to DA_Mar, CTRL_Mar produced an overall stronger precipitation indicated by the larger area with precipitation rate above 1 mm h⁻¹ from central to southern South Korea. The threat score (TS) can provide a point-by-point evaluation on precipitation forecast. TSs were calculated for continental South Korea at 16 UTC 7 March using the following equation 390 based on Xiao et al. (2005):

$$TS = \frac{C}{F+R-C} \quad (2)$$

where C is the number of correct forecast events; F is the number of forecast events; and R is the number of observed events in South Korean Surface Analysis data. The TSs of CTRL_Mar are 0.62, 0.51, and 0.09 for threshold values of 1, 2, and 3 mm hr⁻¹, respectively. A more accurate precipitation forecast was produced by DA_Mar with TSs of 0.77, 0.57, and 0.15 for threshold values of 1, 2, and 3 mm hr⁻¹, respectively.

Low level moisture flux convergence is an important condition for precipitation in winter storms (Hartung et al. 2011). The moisture flux divergence ($Q \cdot \overline{DIV}$) and moisture transport ($Q \cdot \overline{V}$) at 925 hPa from the CTRL_Mar and DA_Mar were plotted in Fig. 10. In both CTRL_Mar and DA_Mar, strong moisture convergence regions (negative values in the color of blue in Fig. 10a, b) correspond well with the snowfall (Fig. 9b, c) produced over the southern end of Korean Peninsula and in the Korean Strait. Moisture convergence in both simulations was generally weak over the Korean Peninsula which led to light to moderate snowfall over most of the area. A closer look at DA_Mar shows that data assimilation helped reduce moisture convergence near 128° E and 36° N (Fig. 10b), agreeing with smaller area of precipitation > 2 mm hr⁻¹ (Fig. 9c). At the southern end of Korean Peninsula, CTRL_Mar also produced stronger moisture convergence (Fig. 10a) compared to DA_Mar (Fig. 10b) which is consistent with the smaller precipitation amount in Fig. 9c. Similarly, low level moisture transport in CTRL_Mar was characterized by larger values from central to southern South Korea (Fig. 10c) than DA_Mar (Fig. 10d). This is especially apparent in the region near 128° E and 36° N and along the southern coast line.

The snowstorm moved northeastward and precipitation related to the system firstly appeared in the southwest end of South Korea at 08 UTC 7 March. Large amount of precipitation in South Korea concentrated between 17 UTC 7 and 00 UTC 8 March. In Fig. 11, 24-h accumulated precipitation from 06 UTC 7 to 06 UTC 8 March is plotted for the observation and compared with the numerical experiments. From the South Korean Surface Analysis, there were over 20 mm snowfall produced in the southern provinces and cities with over 40 mm snowfall along the coast in South Gyeongsang Province. As shown in Fig. 11b and 11c, both CTRL_Mar and DA_Mar overpredicted the precipitation amount with >15 mm precipitation covered almost the entire South Korea. Overestimation is especially apparent in CTRL_Mar which predicted precipitation of >40 mm over most area of the central and southern provinces. Heavy snowfall above 70 mm with the extreme value of 95 mm was predicted along the southeastern coast of Ulsan and North Gyeongsang province in CTRL_Mar. In comparison, DA_Mar predicted a much smaller area with precipitation exceeding 40 mm. In addition, the maximum precipitation was 82 mm over coast of Ulsan, 13 mm lower than CTRL_Mar. The Probability Density Function (PDF) of 24-h precipitation amount was calculated with bin-size of 2 mm over South Korea where the surface analysis data is available. It is shown

that 13.5% of the observed area in South Korea had light precipitation of 0-2 mm. 77.2% of the entire area observed snowfall of <20 mm, 19.6% of the area had precipitation of 20-40 mm, and only 3.2 % of the area experienced precipitation of >40 mm in the 24 hours. Both CTRL_Mar and DA_Mar predicted much lower percentage of area (i.e., 2.5% and 2.2%, respectively) for light precipitation of 0-2 mm. In CTRL_Mar, the peak precipitation probability was predicted at 42 mm for 6.7% of the area in South Korea. Snowfall of <20 mm occurred at 19.3% of the entire area which is 57.9% smaller than the observation. 20-40 mm snowfall was predicted in CTRL_Mar for 39.4% of the area, 19.8% higher than the observed value. Precipitation of >40 mm was generated for 41.3% of the area which is 38.1% larger than the observation. DA_Mar performed better than CTRL_Mar with an overall lower precipitation amount. The peak precipitation probability was at 36 mm for 8.8% of the area. Light snowfall below 20 mm was predicted for 23% of the area, 20-40 mm snowfall for 60% of the area, and >40 mm for 17% of the area, indicating less overprediction. Besides the model validation, it is also of our interest to understand the accuracy of GPM observed precipitation for snowstorms over the Korean peninsula. As ICE-POP 2018 program is a part of the GPM ground validation effort, it is of interest to examine the accuracy of GPM data for solid precipitation over complex terrain by comparing the precipitation amount observed by the South Korean Surface Analysis with the GPM IMERG product for the two snowstorm events over South Korea. The IMERG incorporates observations from GPM and partner satellite microwave and infrared (IR) precipitation estimates to form a Level 3 gridded global precipitation product with spatial resolution of $0.1^\circ \times 0.1^\circ$ and temporal resolutions of 30 minutes. Figure 11d shows 24-h accumulated precipitation between 06 UTC 7 and 06 UTC 8 March from IMERG Final Run. Comparing with the South Korean Surface Analysis data, IMERG produced comparable amount of precipitation in northern South Korea and overall larger precipitation amount over central South Korea. The strong precipitation center of >35 mm in IMERG was to the northeast of the one observed in South Gyeongsang Province by South Korean Surface Analysis. An overestimated precipitation center exceeding 35 mm was also presented in west coast of South Korea by IMERG. These features were reflected in the PDF of IMERG precipitation by the much larger probability for precipitation from 20 to 40 mm and much smaller probability for precipitation from 2 to 14 mm.

3.2. Case Study for February 27-28 Snowstorm Event

The above results indicate a positive impact of the GPM-retrieved surface meteorology data on the short-term forecast of the March 7-8 case. The assessment of data assimilation result for the February case will be discussed in this section.

Figure 12 shows the surface temperature, relative humidity, and wind speed in model background compared with O – B and A – B from DA_Feb at 09 UTC 27 February 2018. The GPM-retrieved observation

at this time is available for a large part of Bohai Sea and the eastern half of Yellow Sea and East China Sea. The observation also covers Sea of Japan and western North Pacific Ocean. From Figs. 12b and 12e, the observed surface air was generally warmer in Bohai Sea and colder and drier in Yellow Sea than the model background. Over most of the regions in Sea of Japan and western North Pacific Ocean, surface air was roughly >1 °C warmer but with lower relative humidity (by up to 30%) than the model background. After data assimilation, positive increments in surface temperature were produced over Bohai Sea, Sea of Japan, as well as western North Pacific Ocean with maximum increase of 3.5 °C. In Yellow Sea, negative increments in surface temperature and specific humidity were produced when the data was assimilated (Fig. 12c,f). A decrease in relative humidity was produced over north and central Sea of Japan and most area of western North Pacific Ocean with minimum value of -20%. An increase in relative humidity was created over southern Sea of Japan as well as in East China Sea where more humid observation was found. For surface wind speed, GPM-retrieved observation (Fig. 12h) was generally lower than the background over Bohai Sea, Yellow Sea, and East China Sea, and higher in Sea of Japan and western North Pacific Ocean. After data assimilation, areas of decreased wind speed were found in Bohai Sea, Yellow Sea, and East China Sea. Areas of increased surface wind speed have been produced in western North Pacific Ocean with magnitude up to 3.5 m s^{-1} .

Even though the positive impact of data assimilation is not as significant as the one shown in the March case, it is found that surface temperature forecast was also improved for the February 27-28 event with data assimilation. The RMSEs of 2-m temperature calculated over South Korea from 12 UTC 27 February to 00 UTC 01 March 2018 were listed in Table 2. At 12 UTC 27 February, the RMSE in DA_Mar equals that in CTRL_Feb. From 18 UTC 27 to 00 UTC 28 February, RMSEs in DA_Feb were very close to (0.01 °C difference) CTRL_Feb. From 06 UTC to 18 UTC 28 February, DA_Feb provided smaller RMSEs than CTRL_Feb, implying more skillful forecast. At the end of the simulation period, both CTRL_Feb and DA_Feb produced a larger RMSE than most of the previous times but with a smaller value in CTRL_Feb than DA_Feb (2.59 vs. 2.64). Figure 13 shows 2-m temperature from the South Korean Surface Analysis compared with forecasts from CTRL_Feb and DA_Feb at 18 UTC 28 February 2018. Generally, surface temperature over northern to central South Korea was around 0-4 °C at this time and 4-6 °C in the southern region. Warmer temperature of 6-8 °C was observed along Southern coast. Colder temperature (<-2 °C) was observed along the Taebaek Mountains. Temperature forecast in CTRL_Feb was quite similar to DA_Feb at this time. In the southern regions, predicted temperature was generally >2 °C colder than the observation. The apparent features also include the elongated area with cold air along the Taebaek Mountain range where temperature below -2 °C was produced in DA_Feb and below -4 °C in CTRL_Feb. DA_Feb outperformed CTRL_Feb with a smaller area of cold temperature with smaller extreme value along the Taebaek Mountains.

Figure 14 displays 24-h accumulated precipitation from 21 UTC 27 to 21 UTC 28 February 2018 observed by South Korean Surface Analysis and compared with the results from CTRL_Feb and DA_Feb. It is indicated in Fig. 14a that widespread precipitation >15 mm was generated across South Korea in 24-h with extreme precipitation of 184 mm over Jeju Island. Snowfall over 40 mm was produced in the 24 hours along the southeast coast of South Korea and the northeast coast above 36.5° N. From Fig. 14b and 14c, the precipitation pattern in DA_Feb is similar to CTRL_Feb. Both CTRL_Feb and DA_Feb produced widespread precipitation with regions of snowfall over 40 mm in central South Korea and along the east coast and the south coast. When compared with the South Korean Surface Analysis, both CTRL_Feb and DA_Feb overestimated the precipitation amount which is reflected by the much larger size of the areas with precipitation over 40 mm. Comparing to CTRL_Feb, the area of snowfall over 40 mm in DA_Feb was smaller and the extreme values in heavy precipitating centers were also lower. This overestimation is illustrated in the PDF of precipitation in Fig. 14d. The highest precipitation probability was at 22 mm for 6.6% of the area in observation, 28 mm for 7.8% of the area in CTRL_Feb, and 26 mm for 8.6% of the area in DA_Feb. It was observed that 55% of the entire area with 0-20 mm precipitation, 40% of the area with 20-40 mm, and 5% of the area with > 40 mm. Both CTRL_Feb and DA_Feb predicted less area of light snowfall and more area of moderate to heavy snowfall. This is especially apparent in CTRL_Feb. Light snowfall of 0-20 mm was predicted for 26% of the area which is 29% lower than observation. 59% of the area was predicted to have 20-40 mm snowfall, indicating 19% higher than observation. There were 15% of the area with > 40 mm precipitation which is 10% higher than the observed value. DA_Feb generally performed better than CTRL_Feb with higher occurrence of light to moderate snowfall and lower occurrence of heavy snowfall. 30% of the area was predicted with 0-20 mm, 61% of the area with 20-40 mm, and 9% of the area with snowfall of >40 mm. Figure 14d shows GPM IMERG Final Run 24-h accumulated precipitation from 21 UTC 27 to 21 UTC 28 February. IMERG precipitation was above 35-40 mm over most area of South Korea, indicating an apparent (~10 mm) widespread overestimate of precipitation for this snowstorm when comparing with the South Korean Surface Analysis. In the plot of PDFs of precipitation, this is reflected by the much larger probability for precipitation from 35 to 80 mm and much smaller probability for precipitation from 0 to 28 mm.

4. Discussion and Conclusion

In this research, the GPM-retrieved ocean surface meteorology data has been assimilated with the community GSI v3.6 for two winter storm events during the ICE-POP 2018 field campaign. WRF ARW model simulations were conducted for the two cases to investigate the impact of the retrieved data on winter storm forecast. The objectives of the current research are to investigate the forecast ability of snowstorm events

over complex terrain with the WRF model and evaluate the assimilation of the passive microwave derived surface meteorology on the short-term forecast of the snowstorm events.

The results indicate that large impact of the retrieved surface meteorology data has been produced on surface temperature, moisture, and wind speed fields in the initial condition (Figs. 6 and 12). While clear biases remain in the model analyses over land, the assimilation of the surface meteorology does act to bring the analysis closer to the surface observations. Strong model adjustment was found within 1-3 hours after data assimilation, which is commonly seen when surface data only is assimilated into the initial condition. Positive impact of the data on short-term forecasts of precipitation and temperature was found for both cases when compared to South Korean Surface Analysis. Larger positive impact was found for the March 7-8 case (Figs. 8-9,11 and Table 2), while the impact of the retrieval product was slightly smaller for the February 27-28 case (Figs. 13-14 and Table 2). A closer look at Figs. 6 and 12 shows a larger difference between the background and observation for the February case than the March case, which may partially explain the smaller improvement in the forecast of the February event. In addition, although the synoptic pattern of both winter events belongs to warm low type, the synoptic configurations of the two surface low pressure systems were unlike. Different kinematic and thermodynamic processes involved in the two cases could be another contributing factor for the difference in data assimilation effect. Also, since observational data varies with time and only covers a part of Bohai Sea, Yellow Sea, Sea of Japan and western North Pacific Ocean at most of the times, the undersampling of retrieved product to the individual storm and important atmospheric structures critical to the development of the storm may be an important reason for the different effect of data assimilation. Another interesting finding from this research is that IMERG tends to overestimate 24-h surface precipitation amount for both snowstorm events with the February case being a more apparent example. With only two cases, it may be too early to draw any conclusions, but it might be an interesting question for the GPM science community to investigate.

The conclusions in this study are only based on two case studies. More experiments and continuous data assimilation with more cases are required to produce a more thorough evaluation of the statistical significance of the GPM-retrieved surface meteorology data assimilation. Furthermore, temperature departure was seen to be skewed (Fig. 5d) to the positive side and specific humidity departure to the negative side (Fig. 5e). Outliers were seen in the retrieved surface temperature, specific humidity, and wind speed data. It might be appropriate to adopt a more rigorous gross check and data validation to retain valid data and remove observations that are largely skewed from the normal distribution of background departures. In future studies, more examinations and tests in the quality control and potentially adding a bias correction to the retrieved surface condition data may be a way to bring further improvement in precipitation forecast. In addition, the present study assimilated the GPM-retrieved surface meteorology data only with the conventional data. It is

555 of great interest to assimilate this observational type together with other types of observations obtained from the ICE-POP mission (e.g., radiosondes, radar observations, wind profilers) in which more information above the surface was included. This may provide a clearer understanding on how this type of observation could help to better depict the true state of atmosphere and hence benefit precipitation forecast when combined with other types of observational data.

560

Code and data availability. The community WRF model and the GSI data assimilation system can be accessed at <https://www2.mmm.ucar.edu/wrf/users/> and <https://dtcenter.org/com-GSI/users/>, respectively. GPM satellite rainfall data is available at <https://pmm.nasa.gov/data-access/downloads/gpm>. The prebufr data can be downloaded from <http://rda.ucar.edu/data/ds337.0>. The GPM-retrieved ocean surface meteorology data are available online (<https://doi.org/10.5281/zenodo.5597153>; Roberts et al. 2021). Any additional information related to this paper may be requested from the corresponding author.

565

Author contributions. Authors XL, WAP, JBR, JLC, CRH developed the research idea and modeling and data assimilation framework. XL and JS developed the data assimilation procedure and conducted the experiments. JBR provided and processed the GPM-retrieved surface meteorology data. XL analyzed the results and WAP, JLC, CRH assisted in interpretation of the results. GL provided the South Korean Surface Analysis dataset and assisted JLC with analysis of the snowstorm events. All authors participated in writing of the manuscript.

570

575 **Competing interests.** The authors declare that they have no conflict of interest.

Acknowledgments. We gratefully acknowledge funding provided for this research by the Earth Science Division (Dr. Tsengdar Lee) at NASA Headquarters as part of the NASA Short-term Prediction Research and Transition Center at Marshall Space Flight Center and the NASA Ground Validation component of the NASA-JAXA GPM mission (Dr. Gayle Skofronick-Jackson). The authors would like to thank Drs. GyuWon Lee and Soorok Ryu at Kyungpook National University for providing the South Korean Surface Analysis dataset. The authors would like to express their appreciations to the participants in the World Weather Research Programme Research Development Project and Forecast Demonstration Project, International Collaborative Experiments for Pyeongchang 2018 Olympic and Paralympic winter games (ICE-POP 2018) hosted by the Korea Meteorological Administration. The authors would like to thank the anonymous reviewers for a number of helpful comments that improved the overall quality of this paper.

585

Financial support. This research was supported by the Earth Science Division (Dr. Tsengdar Lee) at NASA
590 Headquarters as part of the NASA Short-term Prediction Research and Transition Center at Marshall Space
Flight Center and the NASA Ground Validation component of the NASA-JAXA GPM mission (Dr. Gayle
Skofronick-Jackson).

References

- Alcott, T., and Steenburgh, W.: Snow-to-Liquid Ratio Variability and Prediction at a High-Elevation Site in
595 Utah's Wasatch Mountains, *Wea. Forecasting*, 25, 323–337,
<https://doi.org/10.1175/2009WAF2222311.1>, 2010.
- Berg, W., Kroodsma, R., Kummerow, C., McKague, D., Berg, W., Kroodsma, R., Kummerow, C. D., and
McKague, D. S.: Fundamental Climate Data Records of Microwave Brightness Temperatures, *Remote
Sens.*, 10(8), 1306, doi:10.3390/rs10081306, 2018.
- 600 Call, D. A.: Changes in ice storm impacts over time: 1886–2000, *Wea. Climate. Soc.*, 2, 23–35.
<https://doi.org/10.1175/2009WCAS1013.1>, 2010.
- Chang, C.P., Wang, Z., and Hendon, H.: The Asian winter monsoon. In: *The Asian Monsoon*, Springer Praxis
Books, Springer, Berlin, Heidelberg, https://doi.org/10.1007/3-540-37722-0_3, 2006.
- Changnon, S. A.: Characteristics of ice storms in the United States, *J. Appl. Meteor.*, 42, 630–639.
605 [https://doi.org/10.1175/1520-0450\(2003\)042<0630:COISIT>2.0.CO;2](https://doi.org/10.1175/1520-0450(2003)042<0630:COISIT>2.0.CO;2), 2003.
- Changnon, S. A.: Catastrophic winter storms: An escalating problem, *Climatic Change*, 84, 131–139.,
<https://doi.org/10.1007/s10584-007-9289-5>, 2007.
- Chen, F., and Dudhia, J.: Coupling an advanced land-surface/ hydrology model with the Penn State/ NCAR
MM5 modeling system. Part I: Model description and implementation, *Mon. Wea. Rev.*, 129, 569–585,
610 [https://doi.org/10.1175/1520-0493\(2001\)129<0569:CAALSH>2.0.CO;2](https://doi.org/10.1175/1520-0493(2001)129<0569:CAALSH>2.0.CO;2), 2001.
- Chou, M.-D., and Suarez, M. J.: A solar radiation parameterization for atmospheric studies, NASA Tech.
Memo. 104606, NASA, Greenbelt, MD., 40pp, <https://gmao.gsfc.nasa.gov/pubs/docs/Chou136.pdf>,
1999.
- Cucurull, L., Vandenberghe, F., Barker, D., Vilaclara, E., and Rius, A.: Three-Dimensional Variational Data
615 Assimilation of Ground-Based GPS ZTD and Meteorological Observations during the 14 December
2001 Storm Event over the Western Mediterranean Sea, *Mon. Wea. Rev.*, 132, 749–763, 2004.
- Curry, J. A., Bentamy, A., Bourassa, M., Bourras, D., Bradley, E., Brunke, M., Castro, S., Chou, S., Clayson,
C., Emery, W., Eymard, L., Cairall, C., Kubota, M., Lin, B., Perrie, W., Reeder, R., Renfrew, I., Rossow,
W., Schulz, J., Smith, S., Webster, P., Wick, G., and Zeng, X.: Seaflux, *Bull. Am. Meteorol. Soc.*, 85(3),
620 409–424, doi:10.1175/BAMS-85-3-409, 2004.
- De Ponca, M., Manikin, G. S., Parrish, D. F., Purser, R. J., Wu, W. S., DiMego, G., Derber, J. C., Benjamin,
S., Horel, J. D., Anderson, L., and Colman, B.: The status of the real time mesoscale analysis at NCEP,
Preprints of the 22nd Conference on Weather Analysis and Forecasting/18th Conference on Numerical
Weather Prediction, Park City, UT, 24-29 June 2007, 4A.5,
625 <http://ams.confex.com/ams/pdfpapers/124364.pdf>, 2007.

- Edson, J. B., Jampana, V., Weller, R. A., Bigorre, S. P., Plueddemann, A. J., Fairall, C. W., Miller, S. D., Mahrt, L., Vickers, D., and Hersbach, H.: On the Exchange of Momentum over the Open Ocean, *J. Phys. Oceanogr.*, 43(8), 1589–1610, doi:10.1175/JPO-D-12-0173.1, 2013.
- English, J. M., Kren, A. C., and Peevey, T. R.: Improving winter storm forecasts with observing system simulation experiments (OSSEs). Part II: Evaluating a satellite gap with idealized and targeted dropsondes, *Earth Space Sci.*, 5, 176–196, <https://doi.org/10.1002/2017EA000350>, 2018.
- FEMA: FEMA disaster declarations summaries, FEMA (Data Set), <https://www.fema.gov/api/open/v2/DisasterDeclarationsSummaries>, 2021.
- Fillion, L., Tanguay, M., Lapalme, E., Denis, B., Desgagne, M., Lee, V., Ek, N., Liu, Z., Lajoie, M., Caron, J., and Pagé, C.: The Canadian Regional Data Assimilation and Forecasting System, *Wea. Forecasting*, 25, 1645–1669, <https://doi.org/10.1175/2010WAF2222401.1>, 2010.
- Garvert, M., Woods, C., Colle, B., Mass, C., Hobbs, P., Stoelinga, M., and Wolfe, B.: The 13–14 December 2001 IMPROVE-2 Event. Part II: Comparisons of MM5 Model Simulations of Clouds and Precipitation with Observations, *J. Atmos. Sci.*, 62, 3520–3534, <https://doi.org/10.1175/JAS3551.1>, 2005.
- Gehring, J., Oertel, A., Vignon, É., Jullien, N., Besic, N., and Berne, A.: Microphysics and dynamics of snowfall associated with a warm conveyor belt over Korea, *Atmos. Chem. Phys.*, 20, 7373–7392, doi:10.5194/acp-20-7373-2020, 2020.
- Grell, G. A. and Freitas, S. R.: A scale and aerosol aware stochastic convective parameterization for weather and air quality modeling, *Atmos. Chem. Phys.*, 14, 5233–5250, doi:10.5194/acp-14-5233-2014, 2014.
- Hamill, T., Yang, F., Cardinali, C., and Majumdar, S.: Impact of Targeted Winter Storm Reconnaissance Dropwindsonde Data on Midlatitude Numerical Weather Predictions, *Mon. Wea. Rev.*, 141, 2058–2065, <https://doi.org/10.1175/MWR-D-12-00309.1>, 2013.
- Hartung, D. C., Otkin, J. A., Peterson, R. A., Turner, D. D., and Feltz, W. F.: Assimilation of surface-based boundary-layer profiler observations during a cool season observation system simulation experiment. Part II: Forecast assessment, *Mon. Wea. Rev.*, 139, 2327–2346, <https://doi.org/10.1175/2011MWR3623.1>, 2011.
- Hou, A. Y., Kakar R., Neeck, S., Azarbarzin, A., Kummerow, C., Kojima, M., Oki, R., Nakamura, K., and Iguchi, T.: The Global Precipitation Measurement mission. *Bull. Amer. Meteor. Soc.*, 95, 701–722, doi:<https://doi.org/10.1175/BAMS-D-13-00164.1>, 2014.
- Hu, M., Ge, G., Shao, H., Stark, D., Newman, K., Zhou, C., Beck, J., and Zhang, X.: Grid-point Statistical Interpolation (GSI) User's Guide Version 3.6, NOAA Developmental Testbed Center, 150 pp, https://dtcenter.org/com-GSI/users/docs/users_guide/GSIUserGuide_v3.6.pdf, 2016.
- Janjic, Z. I.: The step-mountain eta coordinate model: further developments of the convection, viscous

sublayer and turbulence closure schemes, *Mon. Wea. Rev.*, 122, 927–945, [https://doi.org/10.1175/1520-0493\(1994\)122<0927:TSMECM>2.0.CO;2](https://doi.org/10.1175/1520-0493(1994)122<0927:TSMECM>2.0.CO;2), 1994.

660

Kain, J., Goss, S., and Baldwin, M.: The Melting Effect as a Factor in Precipitation-Type Forecasting, *Wea. Forecasting*, 15, 700–714, [https://doi.org/10.1175/1520-0434\(2000\)015<0700:TMEAAF>2.0.CO;2](https://doi.org/10.1175/1520-0434(2000)015<0700:TMEAAF>2.0.CO;2), 2000.

665

Kim, S., Kim, H. M., Kim, E.-J., and Shin, H.-C.: Forecast sensitivity to observations for high-impact weather events in the Korean Peninsula (in Korean with English abstract), *Atmosphere*, 23, 171–186, <https://doi.org/10.14191/Atmos.2013.23.2.171>, 2013.

Kim, S.-M., and Kim, H. M.: Adjoint-based observation impact of Advanced Microwave Sounding Unit-A (AMSU-A) on the short-range forecasts in East Asia (in Korean with English abstract), *Atmosphere*, 27, 93–104, <https://doi.org/10.14191/Atmos.2017.27.1.093>, 2017. Kleist, D. T., Parrish, D. F., Derber, J. C., Treadon, R., Wu, W.-S., and Lord, S.: Introduction of the GSI into the NCEPs Global Data Assimilation System, *Wea. Forecasting*, 24, 1691–1705, <https://doi.org/10.1175/2009WAF2222201.1>, 2009.

670

Jackson, D. L., Wick, G., and Bates, J.: Near-surface retrieval of air temperature and specific humidity using multisensor microwave satellite observations, *J. Geophys. Res.*, 111(D10), 1–16, doi:10.1029/2005JD006431., 2006.

675

Lee, H. S., and Yamashita, T.: On the wintertime abnormal storm waves along the east coast of Korea. In: *Asian and Pacific Coasts 2011*, World Scientific, Hong Kong, pp. 1592-1599, doi: 10.1142/9789814366489_0191, 2011.

Lee, J., Son, S.-W., Cho, H.-O., Kim, J., Cha, D.-H., Gyakum, J. R., and Chen, D.: Extratropical cyclones over East Asia: climatology, seasonal cycle, and long-term trend, *Clim. Dyn.*, 54, 1131–1144, doi:10.1007/s00382-019-05048-w, 2020.

680

Lee, Y.-Y., Lim, G.-H., and Kug, J.-S.: Influence of the East Asian winter monsoon on the storm track activity over the North Pacific, *J. Geophys. Res. Atmos.*, 115(D9), doi:10.1029/2009JD012813, 2010.

Mitnik, L. M., Gurvich, I. A., and Pichugin, M. K.: Satellite sensing of intense winter mesocyclones over the Japan Sea, 2011 IEEE Intl. Geosci. Remote Sens. Symp., 2345-2348, doi:10.1109/IGARSS.2011.6049680, 2011.

685

Morrison, H., Thompson, G., and Tatarskii, V.: Impact of cloud microphysics on the development of trailing stratiform precipitation in a simulated squall line: Comparison of one- and two-moment schemes, *Mon. Wea. Rev.*, 137, 991–1007, <https://doi.org/10.1175/2008MWR2556.1>, 2009.

690

NOAA National Centers for Environmental Information (NCEI): U.S. Billion-Dollar Weather and Climate Disasters (2021), NOAA, <https://www.ncdc.noaa.gov/billions/>, doi:10.25921/stkw-7w73, 2021.

- Niziol, T. A., Snyder, W. R., and Waldstreicher, J. S.: Winter weather forecasting throughout the eastern United States. Part IV: Lake effect snow, *Wea. Forecasting*, 10, 61–77, [https://doi.org/10.1175/1520-0434\(1995\)010<0061:WWFTTE>2.0.CO;2](https://doi.org/10.1175/1520-0434(1995)010<0061:WWFTTE>2.0.CO;2), 1995.
- 695 Novak, D. R., Brill, K. F., and Hogsett, W. A.: Using percentiles to communicate snowfall uncertainty, *Wea. Forecasting*, 29, 1259–1265, <https://doi.org/10.1175/WAF-D-14-00019.1>, 2014.
- Novak, D., and Colle, B.: Diagnosing Snowband Predictability Using a Multimodel Ensemble System, *Wea. Forecasting*, 27, 565–585, <https://doi.org/10.1175/WAF-D-11-00047.1>, 2012.
- O’Hara, B., Kaplan, M., and Underwood, S.: Synoptic Climatological Analyses of Extreme Snowfalls in the Sierra Nevada, *Wea. Forecasting*, 24, 1610–1624, <https://doi.org/10.1175/2009WAF2222249.1>, 2009.
- 700 Oh, S.-H., Jeong, W.-M.: Extensive monitoring and intensive analysis of extreme winter-season wave events on the Korean east coast, *J. Coastal Research*, 70(10070), 296-301, doi: 10.2112/SI70-050.1, 2014.
- Peevey, T. R., English, J. M., Cucurull, L., Wang, H., and Kren, A. C.: Improving winter storm forecasts with observing system simulation experiments (OSSEs). Part I: An idealized case study of three U.S. storms, *Mon. Wea. Rev.*, 146, 1341–1366, <https://doi.org/10.1175/MWR-D-17-0160.1>, 2018.
- 705 Petersen, W., Wolff, D., Chandrasekar, V., Roberts, J., and Case, J.: NASA Observations and Modeling during ICE-POP, KMA ICE-POP Meeting, South Korea, 27-30 November 2018. <https://ntrs.nasa.gov/api/citations/20190001414/downloads/20190001414.pdf?attachment=true>, 2018.
- Powers, J. G., Klemp, J., Skamarock, W., Davis, C., Dudhia, J., Gill, D., Coen, J., Gochis, D., Ahmadov, R., Peckham, S., Grell, G., Michalakes, J., Trahan, S., Benjamin, S., Alexander, C., Dimego, G., Wang, W., Schwartz, C., Romine, G., Liu, Z., Snyder, C., Chen, F., Barlage, M., Yu, W., and Duda, M.: The weather research and forecasting model: Overview, system efforts, and future directions, *Bull. Amer. Meteor. Soc.*, 98, 1717–1737, <https://doi.org/10.1175/BAMS-D-15-00308.1>, 2017.
- 710 Ralph, F., Rauber, R., Jewett, B., Kingsmill, D., Pisano, P., Pugnner, P., Rasmussen, R., Reynolds, D., Schlatter, T., Stewart, R., Tracton, S., and Waldstreicher, J.: Improving Short-Term (0–48 h) Cool-Season Quantitative Precipitation Forecasting: Recommendations from a USWRP Workshop, *Bull. Amer. Meteor. Soc.*, 86, 1619–1632, doi:10.1175/BAMS-86-11-1619, 2005.
- 715 Roberts, J. B., Clayson, C. A., Robertson, F. R., and Jackson, D. L.: Predicting near-surface atmospheric variables from Special Sensor Microwave/Imager using neural networks with a first-guess approach, *J. Geophys. Res.*, 115, D19113, doi:10.1029/2009JD013099, 2010.
- 720 Roberts, J., Li, X., Srikishen, J., Case, J., Petersen, W., Lee, G.-W., and Hain, C.: Assimilation of GPM-retrieved Ocean Surface Meteorology Data for Two Snowstorm Events during ICE-POP 2018 – GPM Retrieved Ocean Surface Meteorology Dataset. Zenodo [data set], <https://doi.org/10.5281/zenodo.5597153>, 2021.

- 725 Roller, C., Qian, J.-H., Agel, L., Barlow, M., and Moron, V.: Winter Weather Regimes in the Northeast United States, *J. Climate*, 29, 2963–2980, <https://doi.org/10.1175/JCLI-D-15-0274.1>, 2016.
- Ryu, S., Song, J. J., Kim, Y., Jung, S.-H., Do, Y., and Lee, G.: Spatial Interpolation of Gauge Measured Rainfall Using Compressed Sensing, *Asia-Pacific J. Atmos. Sci.*, 57, 331–345 (2021). <https://doi.org/10.1007/s13143-020-00200-7>, 2020.
- 730 Saslo, S., and Greybush, S. J.: Prediction of lake-effect snow using convection-allowing ensemble forecasts and regional data assimilation, *Wea. Forecasting*, 32, 1727–1744, <https://doi.org/10.1175/WAF-D-16-0206.1>, 2017.
- Schultz, D. M., Steenburgh, W. J., Trapp, R. J., Horel, J., Kingsmill, D. E., Dunn, L. B., Rust, W. D., Cheng, L., Bansemer, A., Cox, J., Daugherty, J., Jorgensen, D. P., Meitín, J., Showell, L., Smull, B. F., Tarp, K., and Trainor, M.: Understanding Utah winter storms: The Intermountain Precipitation Experiment, *Bull. Amer. Meteor. Soc.*, 83, 189–210, [https://doi.org/10.1175/1520-0477\(2002\)083<0189:UUWSTI>2.3.CO;2](https://doi.org/10.1175/1520-0477(2002)083<0189:UUWSTI>2.3.CO;2), 2002.
- 735 Schuur, T., Park, H.-S., Ryzhkov, A., and Reeves, H.: Classification of Precipitation Types during Transitional Winter Weather Using the RUC Model and Polarimetric Radar Retrievals, *J. Appl. Meteor. Climatol.*, 51, 763–779, <https://doi.org/10.1175/JAMC-D-11-091.1>, 2012.
- 740 Skofronick-Jackson, G., Petersen, W., Berg, W., Kidd, C., Stocker, E., Kirschbaum, D., Kakar, R., Braun, S., Huffman, G., Iguchi, T., Kirstetter, P., Kummerow, C., Meneghini, R., Oki, R., Olson, W., Takayabu, Y., Furukawa, K., and Wilheit, T.: The Global Precipitation Measurement (GPM) mission for science and society. *Bull. Amer. Meteor. Soc.*, 98, 1679–1695, doi:<https://doi.org/10.1175/BAMS-D-15-00306.1>, 2017.
- 745 Tomita, H., Hihara, T., and Kubota, M.: Improved Satellite Estimation of Near-Surface Humidity Using Vertical Water Vapor Profile Information, *Geophys. Res. Lett.*, 45(2), 899–906, doi:10.1002/2017GL076384, 2018.
- Tsuboki, K., and Asai, T.: The multi-scale structure and development mechanism of mesoscale cyclones over the Sea of Japan in winter, *J. Meteor. Soc. Japan*, 82(2), 597–621, doi: 10.2151/jmsj.2004.597, 2004.
- 750 Wu, W.-S.: Background error for NCEP’s GSI analysis in regional mode, *Proceeding of the 4th International Symposium on Analysis of Observations in Meteorology and Oceanography*, Prague, Czech Republic, WMO, 18–22 April 2005, 3A.27, 2005.
- Wu, W.-S., Parrish, D. F., and Purser, R. J.: Three-dimensional variational analysis with spatially inhomogeneous covariances, *Mon. Wea. Rev.*, 130, 2905–2916, [https://doi.org/10.1175/1520-0493\(2002\)130<2905:TDVAWS>2.0.CO;2](https://doi.org/10.1175/1520-0493(2002)130<2905:TDVAWS>2.0.CO;2), 2002.
- 755 Xiao, Q., Kuo, Y. H., Sun, J., Lee, W. C., Lim, E., Guo, Y. R., and Barker, D. M.: Assimilation of Doppler

Radar Observations with a Regional 3DVAR System: Impact of Doppler Velocities on Forecasts of a Heavy Rainfall Case. *J. Appl. Meteor.*, 44, 768–788, 2005.

760 Yang, E.-G., and Kim, H. M.: A comparison of variational, ensemble-based, and hybrid data assimilation methods over East Asia for two one-month periods, *Atmos. Res.*, 249, 105257, ISSN 0169-8095, <https://doi.org/10.1016/j.atmosres.2020.105257>, 2021.

Yoshiike, S., and Kawamura, R.: Influence of wintertime large-scale circulation on the explosively developing cyclones over the western North Pacific and their downstream effects, *J. Geophys. Res. Atmos.*, 114(D13), doi: 10.1029/2009JD011820, 2009.

765 Zhang, F., Meng, Z., and Aksoy, A.: Tests of an Ensemble Kalman Filter for Mesoscale and Regional-Scale Data Assimilation. Part I: Perfect Model Experiments, *Mon. Wea. Rev.*, 134, 722–736, <https://doi.org/10.1175/MWR3101.1>, 2006.

Zhang, F., Sun, Y. Q., Magnusson, L., Buizza, R., Lin, S.-J., Chen, J.-H., and Emanuel, K.: What is the predictability limit of midlatitude weather? *J. Atmos. Sci.*, 76, 1077-1091, <https://doi.org/10.1175/JAS-D-18-0269.1>, 2019.

770 Zhang, Y., Sperber, K. R., and Boyle, J. S.: Climatology and interannual variation of the East Asian Winter Monsoon: Results from the 1979–95 NCEP/NCAR reanalysis, *Mon. Wea. Rev.*, 125(10), 2605-2619, doi: 10.1175/1520-0493(1997)125<2605:CAIVOT>2.0.CO;2, 1997.

775 Zhang, Y., Ding, Y., and Li, Q.: A climatology of extratropical cyclones over East Asia during 1958–2001, *Acta. Meteorol. Sin.*, 26, 261–277, doi:10.1007/s13351-012-0301-2, 2012.

Zupanski, M., Zupanski, D., Parrish, D., Rogers, E., and DiMego, G.: Four-Dimensional Variational Data Assimilation for the Blizzard of 2000, *Mon. Wea. Rev.*, 130, 1967–1988, [https://doi.org/10.1175/1520-0493\(2002\)130<1967:FDVDAF>2.0.CO;2](https://doi.org/10.1175/1520-0493(2002)130<1967:FDVDAF>2.0.CO;2), 2002.

780

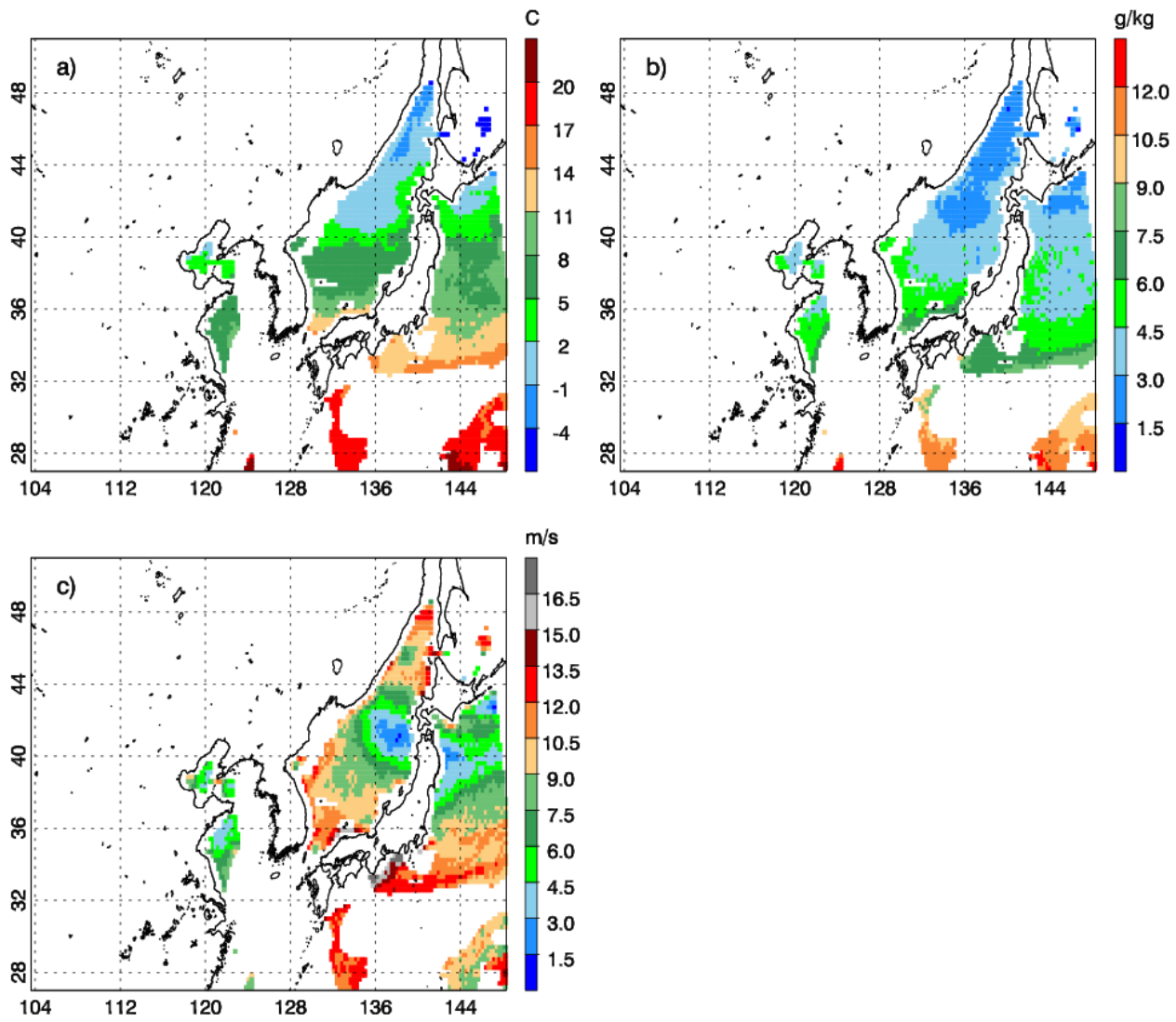
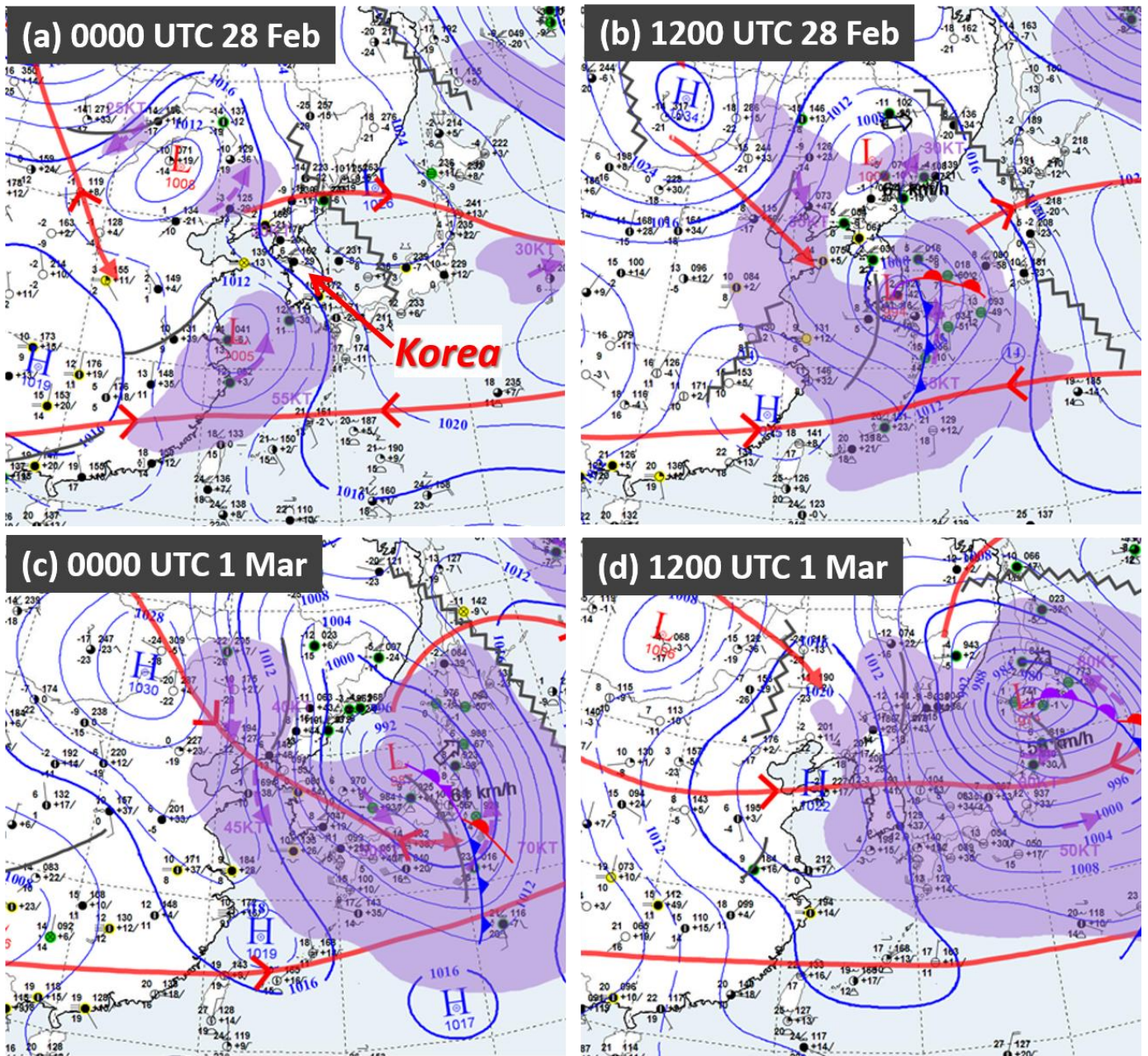
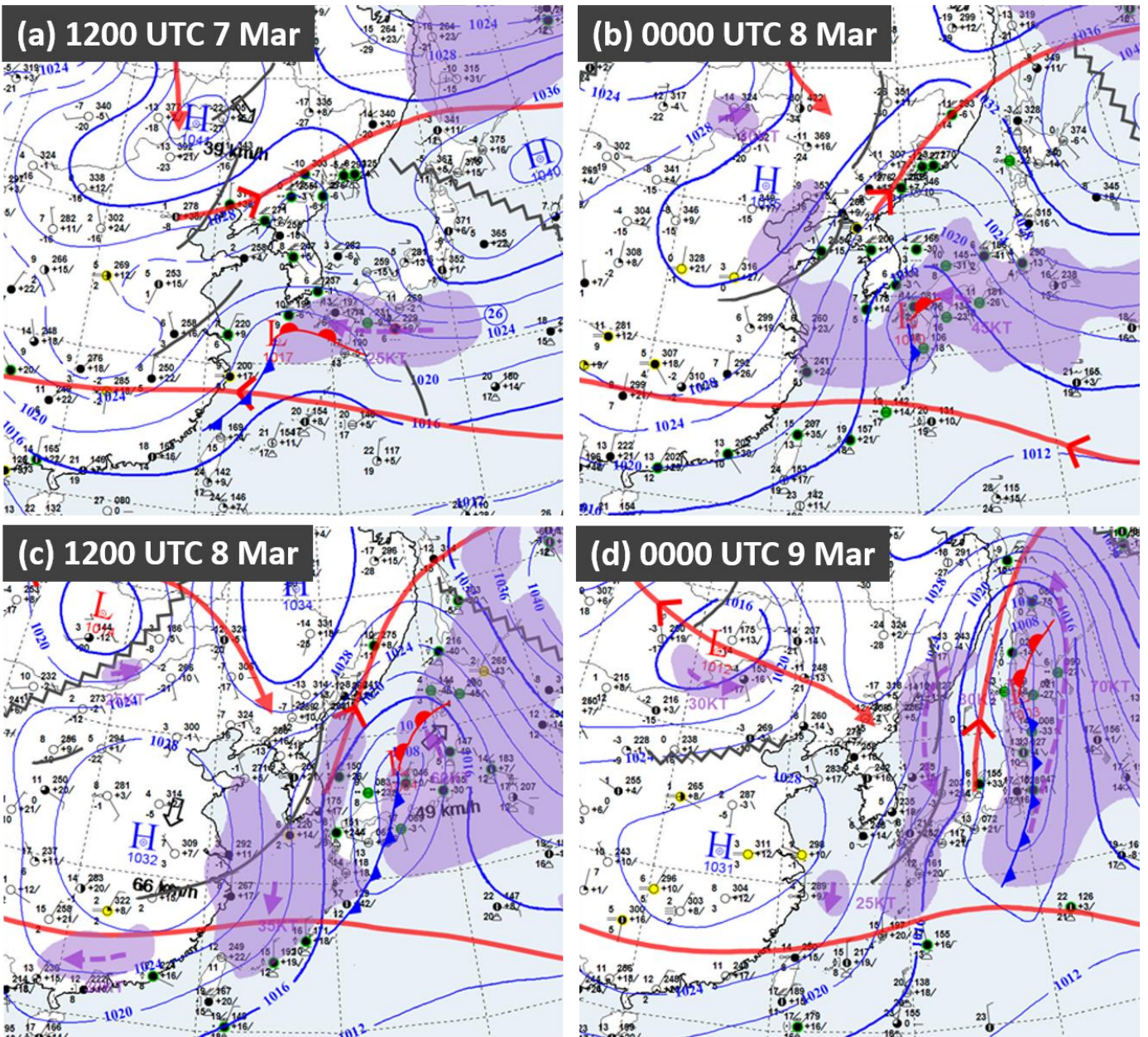


Figure 1. A sample plot of the GPM-retrieved ocean surface meteorology data for a) 2-m temperature [°C], b) 2-m specific humidity [g kg⁻¹], and c) 10-m horizontal wind speed [m s⁻¹] at 09 UTC 7 March 2018.

785



790 Figure 2. Eastern Asia regional surface meteorological analyses by the KMA at 12-hourly intervals, valid at (a) 00 UTC 28 February, (b) 12 UTC 28 February, (c) 00 UTC 1 March, and (d) 12 UTC 1 March 2018.



795 Figure 3. Same as Fig. 2, except valid at (a) 12 UTC 7 March, (b) 00 UTC 8 March, (c) 12 UTC 8 March, and (d) 00 UTC 9 March 2018.

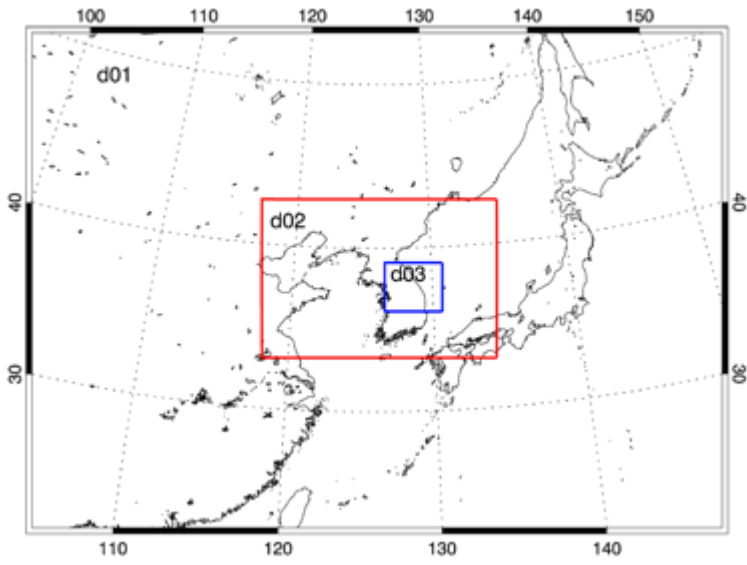


Figure 4. WRF model domain configuration.

800

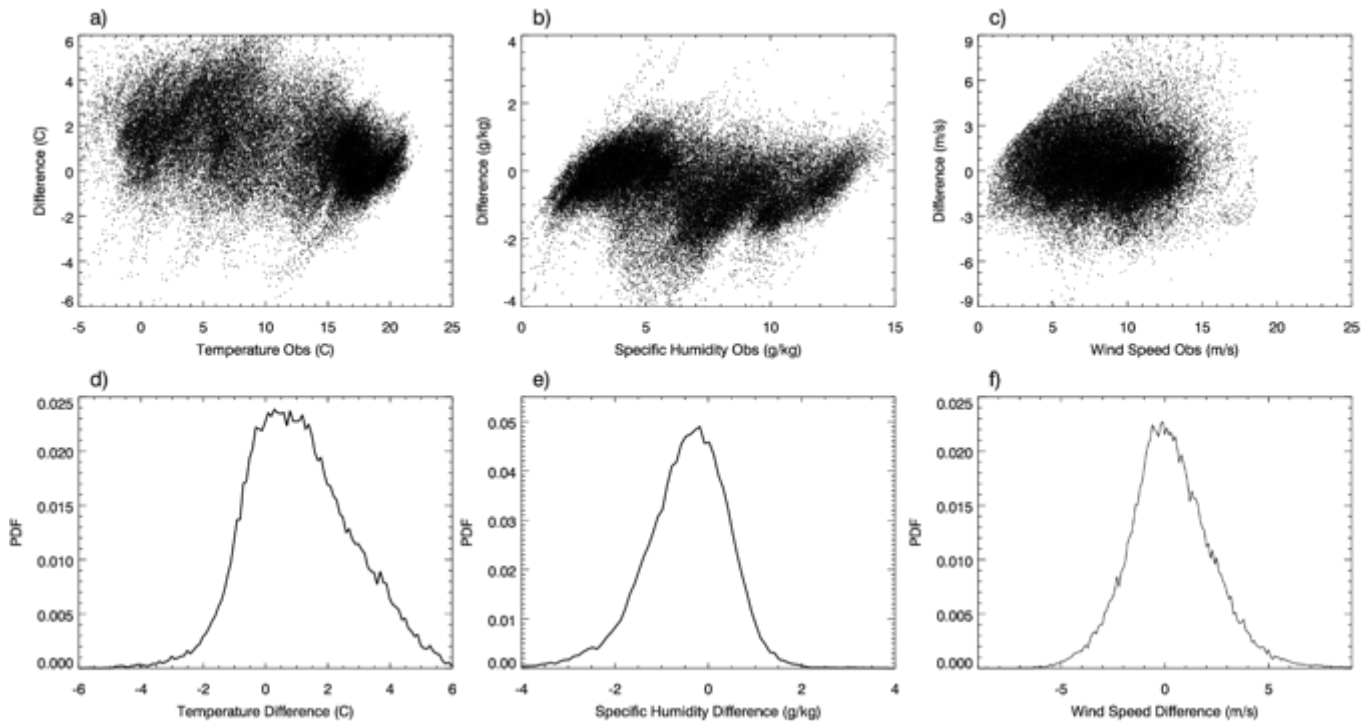
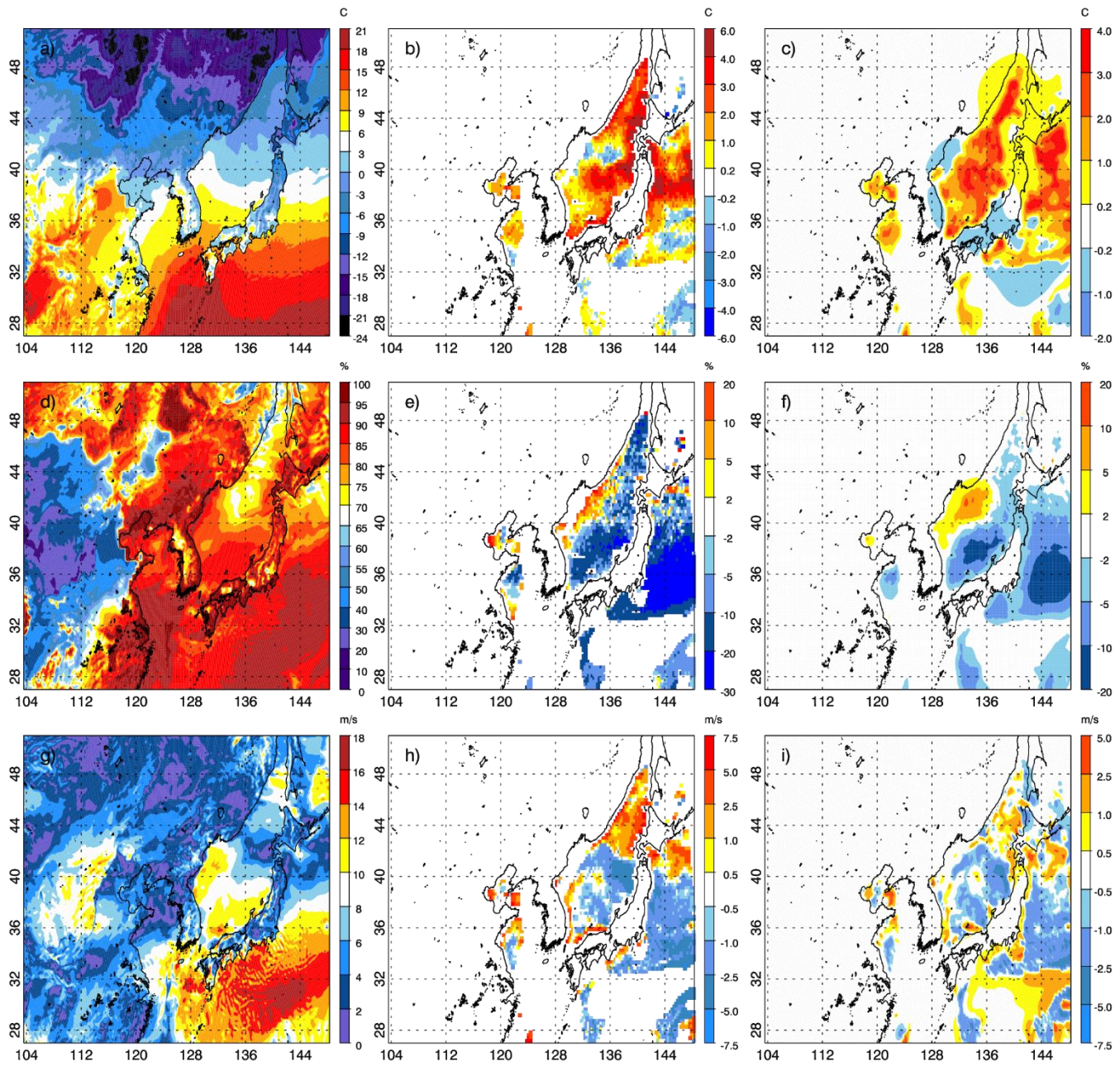


Figure 5. Scatter plot for GPM-retrieved observation vs. the departure between the observation and the model background for a) 2-m temperature [$^{\circ}\text{C}$], b) 2-m specific humidity [g kg^{-1}], and c) 10-m horizontal wind speed [m s^{-1}] from all available data during the data assimilation time windows for the two case studies. Probability density function (PDF) of the d) 2-m temperature departure, b) 2-m specific humidity departure, and c) 10-m horizontal wind speed departure with bin width of 0.1.

805



810 **Figure 6.** WRF Model background for a) 2-m temperature [$^{\circ}\text{C}$], d) 2-m relative humidity [%], and g) 10-m horizontal wind speed [m s^{-1}], difference between observation and model background for b) 2-m temperature, e) 2-m relative humidity, and h) 10-m horizontal wind speed, and difference between data assimilation analysis and the background for c) 2-m temperature, f) 2-m relative humidity, and i) 10-m horizontal wind speed at 09 UTC 7 March 2018.

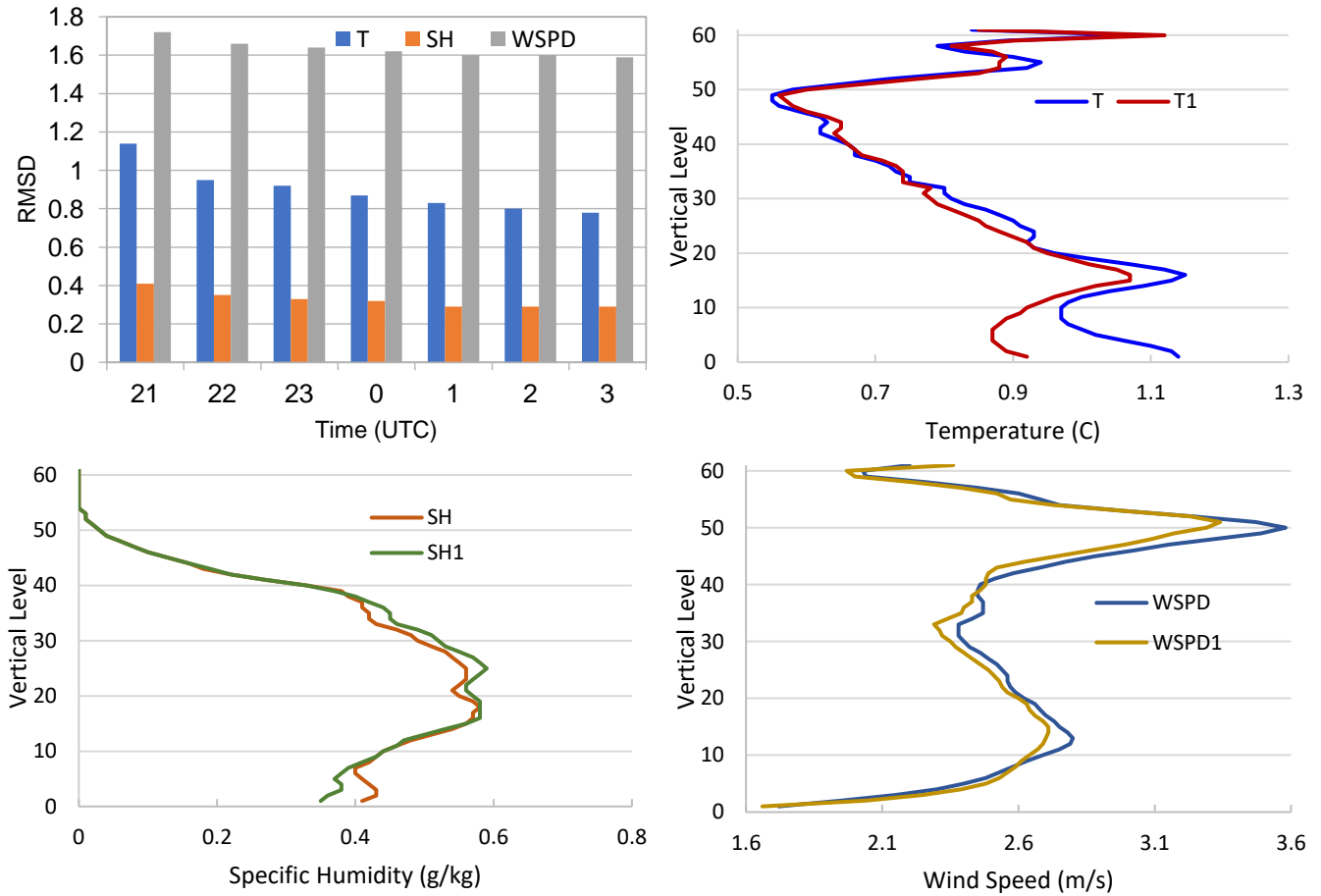
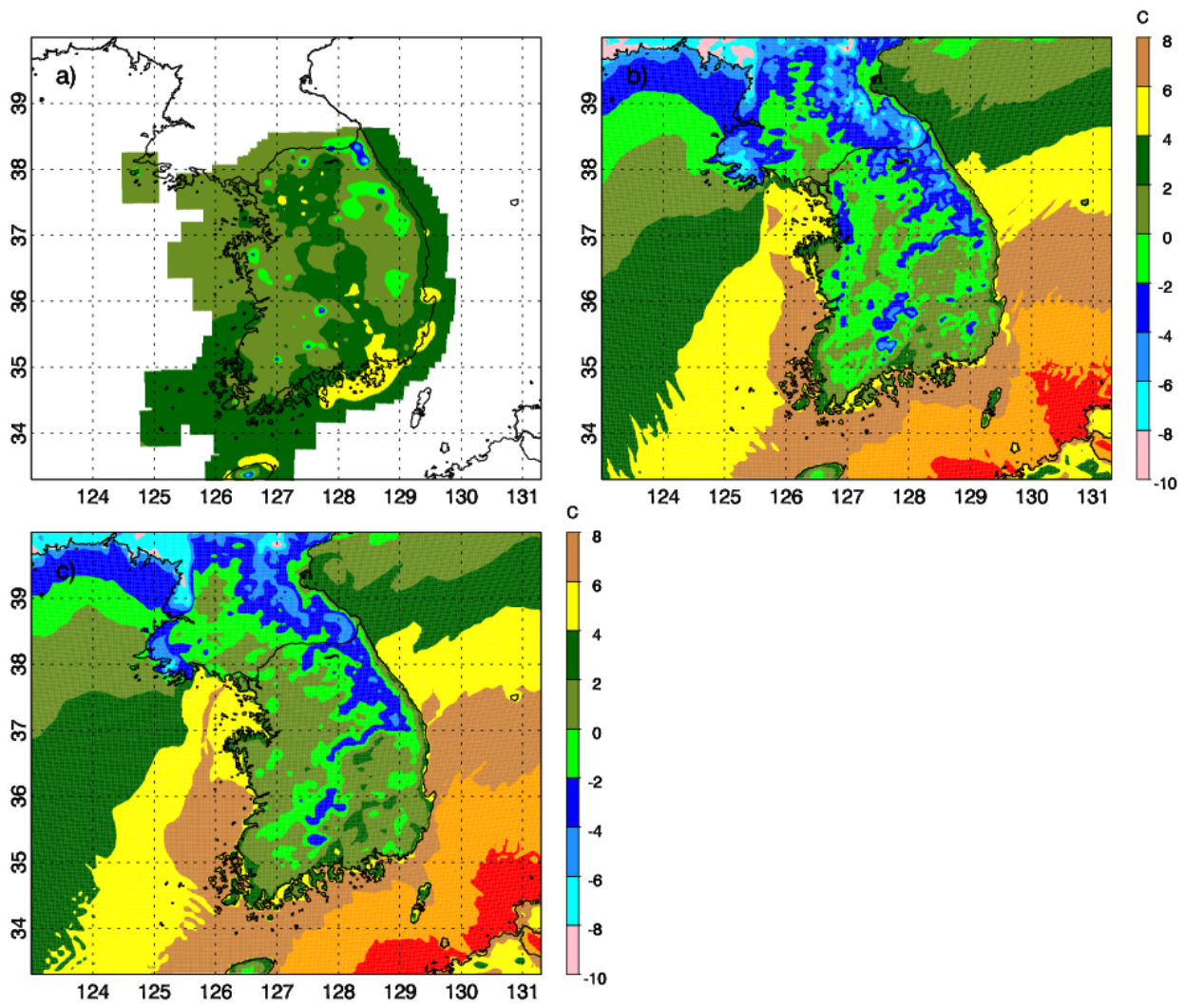


Figure 7. a) Root Mean_Square Difference (RMSD) between DA_Mar and CTRL_Mar for 2-m temperature [$^{\circ}\text{C}$], 2-m specific humidity [g kg^{-1}], and 10-m horizontal wind speed [m s^{-1}] calculated over the model domain from 21 UTC 7 to 03 UTC 8 March 2018, and vertical profiles of RMSD for b) temperature, c) specific humidity, and d) wind speed at 21 UTC (T, SH, and WSPD) and 22 UTC (T1, SH1, and WSPD1) 7 March 2018.



825 Figure 8. 2-m temperature field [$^{\circ}$ C] from a) South Korean Surface Analysis, b) CTRL_Mar, and c) DA_Mar at 15 UTC 8 March 2018.

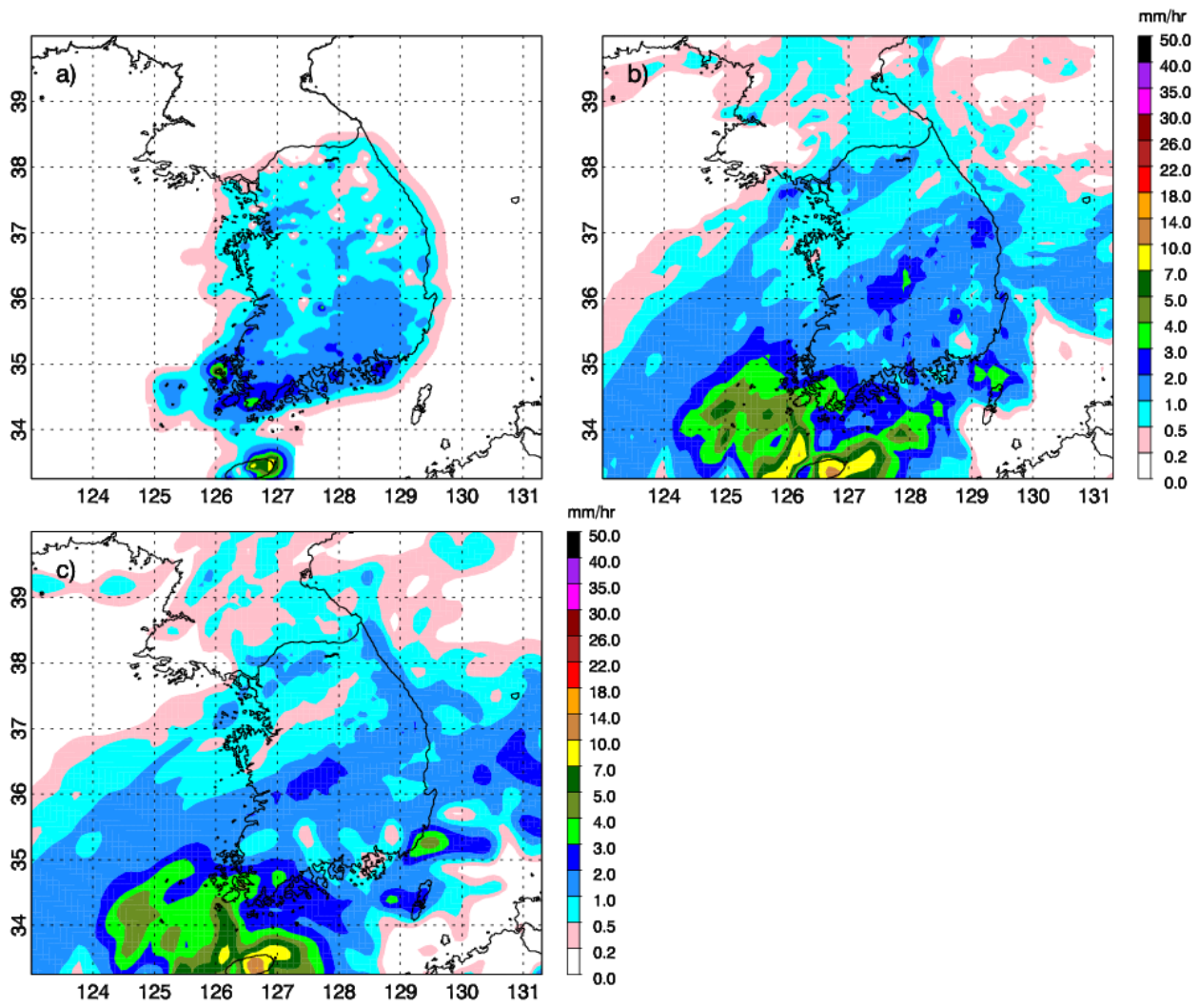
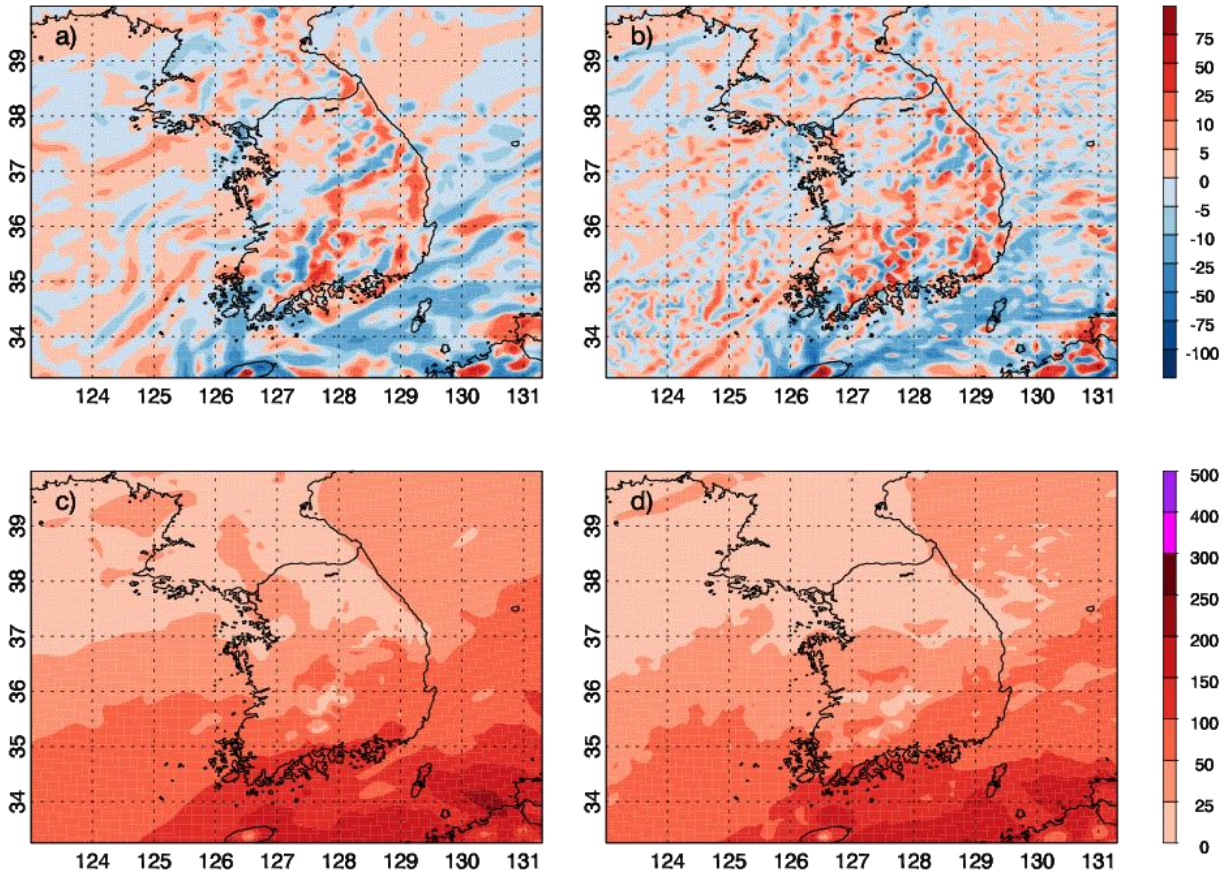


Figure 9. 1-h precipitation (mm h^{-1}) from a) South Korean Surface Analysis, b) CTRL_Mar and c) DA_Mar at 16 UTC 7 March 2018.



830

Figure 10. Moisture flux divergence ($\times 10^{-4} \text{ g kg}^{-1} \text{ s}^{-1}$) for a) CTRL_Mar and b) DA_Mar, and magnitude of moisture transport ($\text{g kg}^{-1} \text{ m s}^{-1}$) for c) CTRL_Mar and c) DA_Mar for 925 hPa and at 16 UTC 7 March 2018.

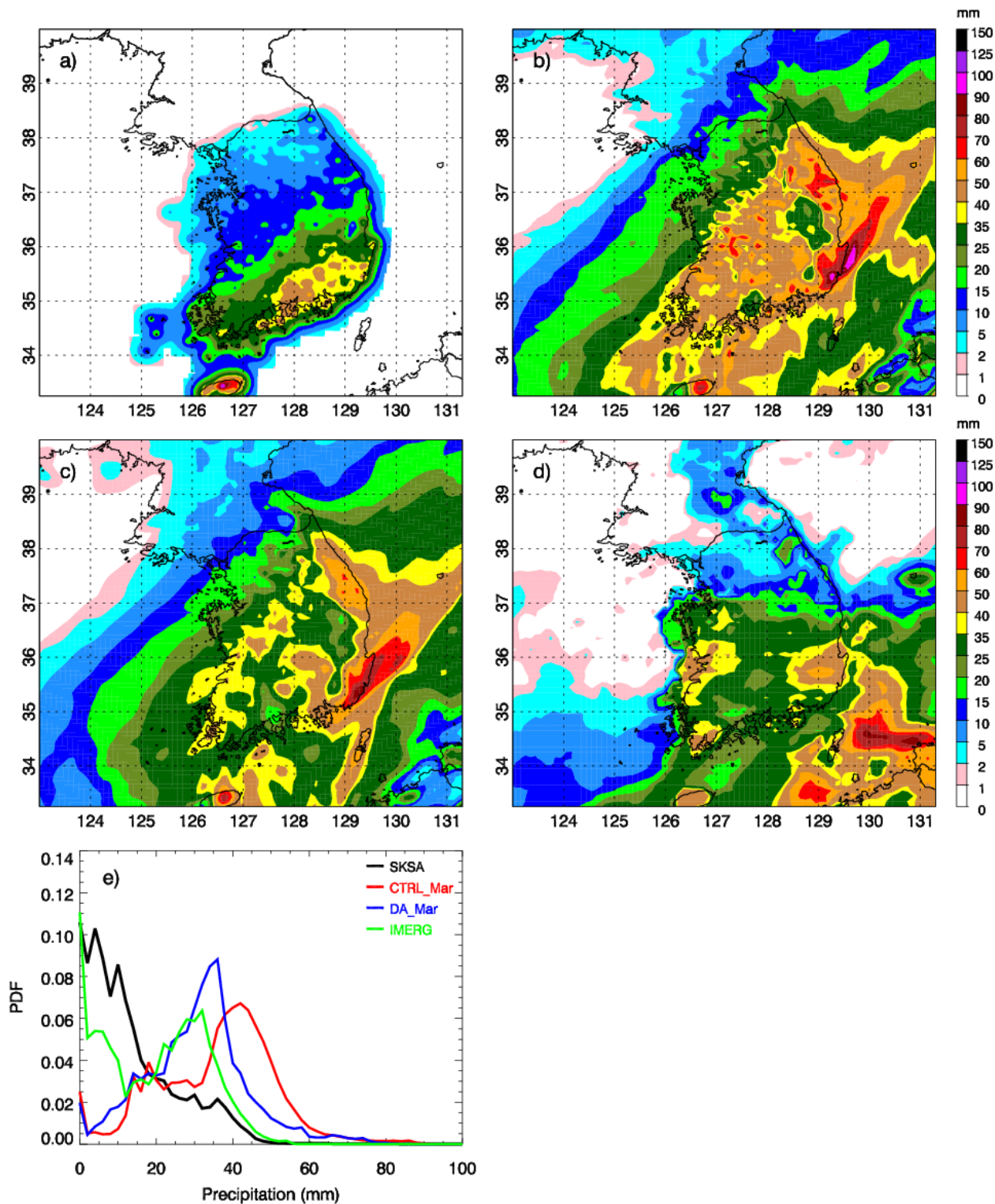
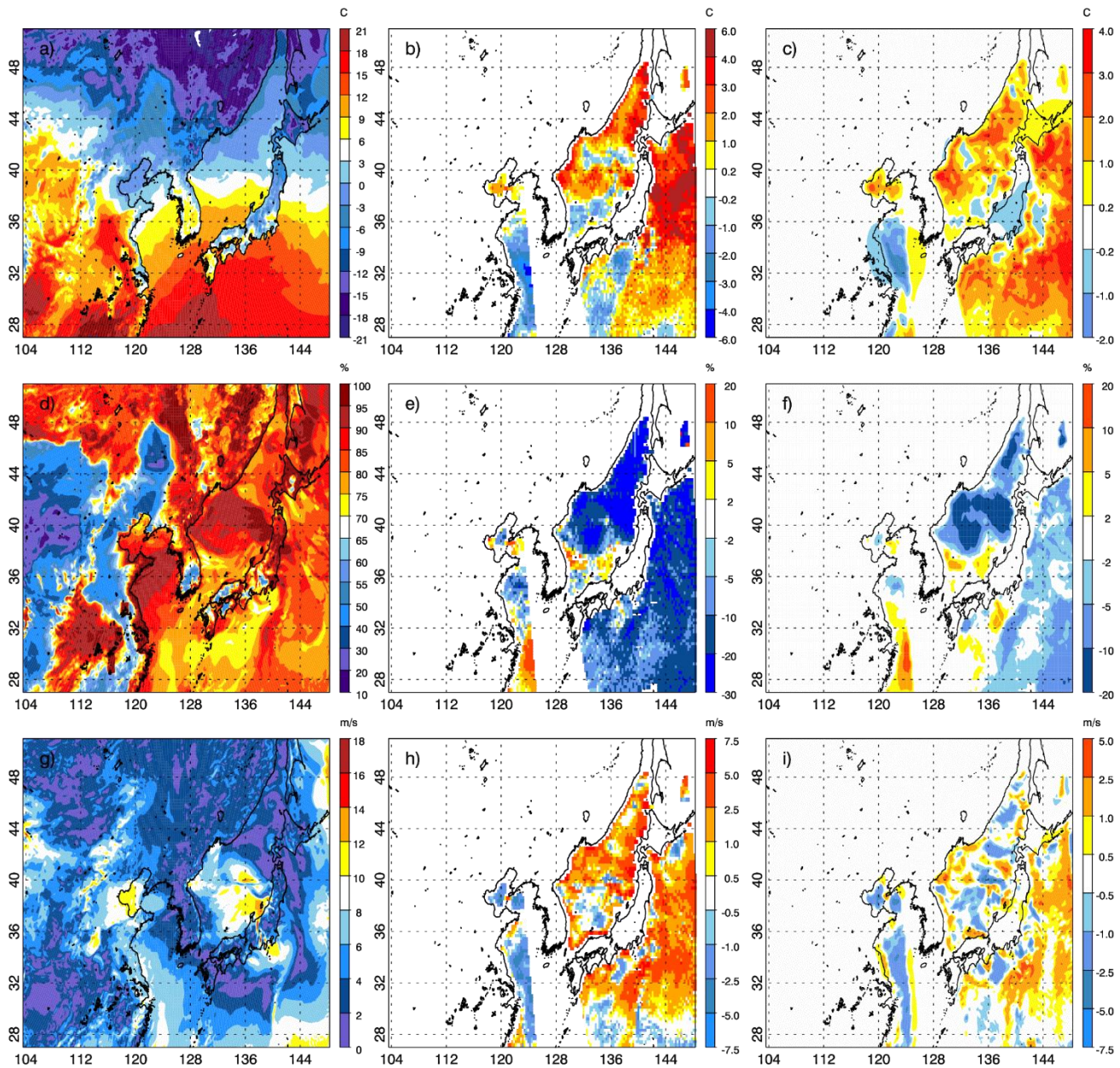


Figure 11. 24-h accumulated precipitation (mm) from a) South Korean Surface Analysis, b) CTRL_Mar, c) DA_Mar, and d) IMERG Final from 06 UTC 7 March to 06 UTC 8 March 2018 and e) probability density function of 24-h accumulated precipitation.



840

Figure 12. WRF Model background fields for a) 2-m temperature [$^{\circ}\text{C}$], d) 2-m relative humidity [%], and g) 10-m horizontal wind speed [m s^{-1}], difference between GPM-retrieved observation and model background fields for b) 2-m temperature, e) 2-m relative humidity, and h) 10-m horizontal wind speed, and difference between data assimilation analysis and model background filed for c) 2-m temperature, f) 2-m relative humidity, and i) 10-m horizontal wind speed at 09 UTC 27 February 2018.

845

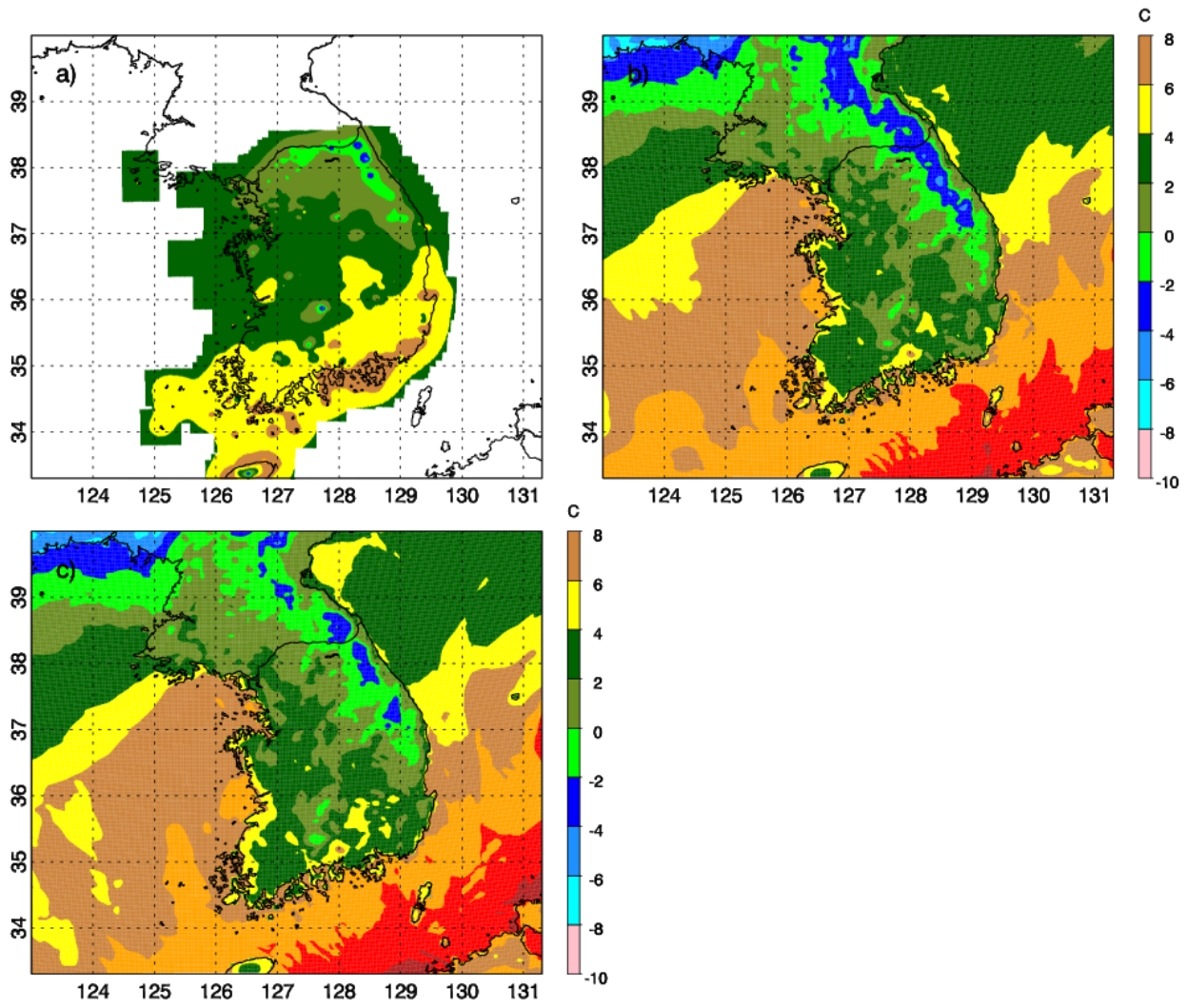
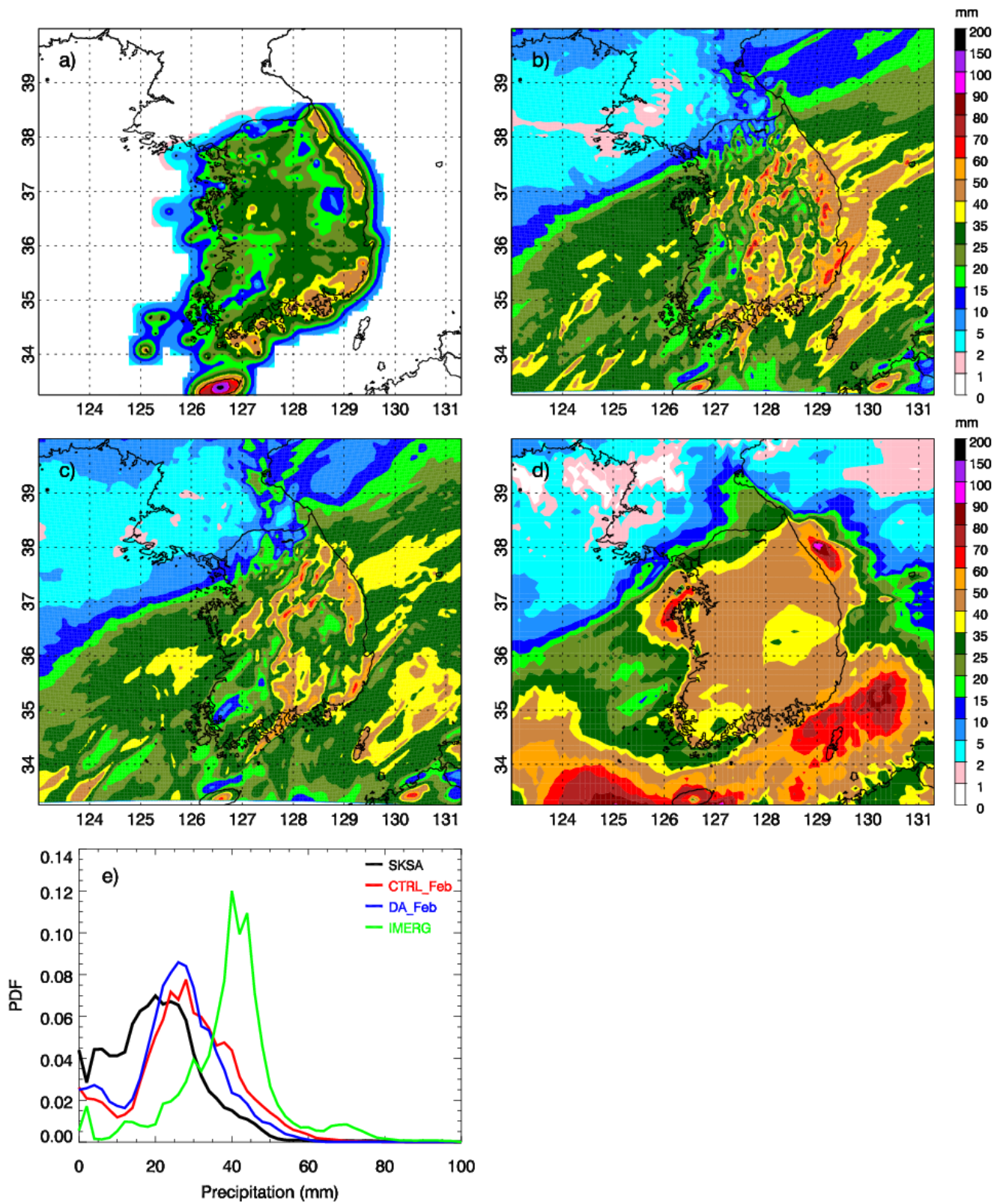


Figure 13. 2-m temperature field [$^{\circ}\text{C}$] from a) South Korean Surface Analysis, b) CTRL_Feb, and c) DA_Feb at 18 UTC 28 February 2018.



850

Figure 14. 24-h accumulated precipitation (mm) from a) South Korean Surface Analysis, b) CTRL_Feb, c) DA_Feb, and d) IMERG Final from 21 UTC 27 to 21 UTC 28 February 2018 and e) probability density function of 24-h accumulated precipitation.

Table 1. Numerical experiments setup.

Experiment	Data	Data Assimilation Time
CTRL_Mar	Conventional data	06, 12, and 18 UTC 7 March 2018 and 00, 06, 12 and 18 UTC 8 March 2018
DA_Mar	GPM-retrieved surface meteorology data + conventional data	06, 09, 12, 18, 21 UTC 7 March 2018 and 00, 06, 09, 12, 18, 21 UTC 8 March 2018
CTRL_Feb	Conventional data	06, 12, and 18 UTC 27 February 2018 and 00, 06, 12 and 18 UTC 28 February 2018
DA_Feb	GPM-retrieved surface meteorology data + conventional data	06, 09, 15, 18, 21 UTC 27 February 2018 and 00, 06, 09, 15, 18, 21 UTC 28 February 2018

Table 2. Root-Mean-Square Error (RMSE) for 2-m temperature [$^{\circ}\text{C}$] forecast over South Korea for difference experiments.

Time	CTRL_Mar	DA_Mar	Time	CTRL_Feb	DA_Feb
12 UTC 03/07/2018	2.65	2.64	12 UTC 02/27/2018	1.95	1.95
18 UTC 03/07/2018	2.82	2.82	18 UTC 02/27/2018	2.10	2.11
00 UTC 03/08/2018	2.73	2.73	00 UTC 02/28/2018	2.33	2.32
06 UTC 03/08/2018	2.33	2.27	06 UTC 02/28/2018	2.11	2.06
12 UTC 03/08/2018	2.15	2.01	12 UTC 02/28/2018	2.70	2.52
18 UTC 03/08/2018	2.85	2.36	18 UTC 02/28/2018	2.29	2.06
00 UTC 03/09/2018	2.47	2.14	00 UTC 03/01/2018	2.59	2.64